

**Development of Multi-Functional Add-On Hybrid Armor Models and  
Designs used for Vehicle Protection**

by

Harshil Hitesh Pisavadia

A thesis submitted in partial fulfillment of the requirements for the degree of

Master of Science

Department of Mechanical Engineering  
University of Alberta

© Harshil Hitesh Pisavadia, 2022

# Abstract

In the first part of this thesis, a validated polyurethane adhesive model is implemented into a system-scale ceramic/armor model for ballistic impact simulations. Here, the trilinear cohesive zone (TCZM) technique is used to simulate the dynamic failure of SikaForce<sup>TM6</sup> 7752-L60 polyurethane adhesive which is used to bond the alumina ceramic layer to the aluminum metal backing in add-on armor vehicle systems. The effect of adhesive thicknesses, manufacturing defects, and strain rates on the armor performance are explored. Armor performance was found to decrease with increasing adhesive thicknesses and defects (trapped air bubbles). Including strain rate terms in the material model increased the overall damage area of the adhesive, thus predicting a decrease in multi-hit capabilities. Overall, novel insights are provided for modelling adhesives using the TCZM technique in ceramic/metal armor systems.

In the second part of this thesis, optical models are developed for micro- and macro-scale polyethylene-based metamaterials for thermal signature management applications. Specifically, micro-scale post and macro-scale lenticular lens designs (single and sandwiched configurations) are explored for achieving thermal radiation control. The micro-scale post design was found to be highly emissive-tuneable through varying post configurations (e.g., post width, height, and spacings). Actively actuating the post configuration through strain modulation allowed to redshift the emissivity. The macro-scale lenticular lens configurations exhibited emissive stability for a range of configurations (e.g., lens radii, height, and strain modulation). In summary, the proposed polyethylene-based metamaterial models inform manufacturers of military vehicles and other equipment on designs for thermal signature management solutions.

# Preface

This thesis titled, “Development of Multi-Functional Add-On Hybrid Armor Models and Designs used for Vehicle Protection” is an original work by Harshil H. Pisavadia.

- Part of Chapter 2 of this thesis has been published in *International Journal of Impact Engineering* as **H. Pisavadia**, G. Toussaint, P. Dolez, and J.D. Hogan, “Cohesive Zone Failure Modelling of Polymeric Adhesives used in Ceramic/Metal Armor”. I was responsible for performing the simulations in this study and the manuscript composition. G. Toussaint contributed to manuscript edits. P. Dolez was the co-supervisory author and was involved with manuscript composition. J.D. Hogan was the supervisory author and was involved with concept formation and manuscript composition.
- Chapter 3 of this thesis is submitted to *Advanced Physics Research* as **H. Pisavadia**, A. Asad, D. Sameoto, P. Dolez, and J.D. Hogan, “Design of Micro- and Macro-scale Polymeric Metamaterial Solutions for Passive and Active Thermal Camouflaging Applications”. I was responsible for performing the simulations in this study and the manuscript composition. A. Asad, and D. Sameoto were involved with concept formulation and manuscript composition. P. Dolez was the co-supervisory author and was involved with manuscript composition. J.D. Hogan was the supervisory author and was involved with concept formation and manuscript composition.

*“You can do anything you put your heart, mind and soul into. Far more than you  
can imagine. Be fearless. Do it.”*

*- LL Cool J*

# Acknowledgments

First and foremost, I would like to extend my appreciation and gratitude towards my supervisor, Dr. James Hogan, for his expertise, ideas, insightful discussions, and mentorship throughout every stage of my entire graduate degree. I would also like to thank him for providing countless opportunities of leadership and collaboration while being flexible towards the completion of my thesis. All of his guidance and support has made me a better researcher and has polished my technical skills.

I am also appreciative to my co-supervisor, Dr. Patricia Dolez, for the excellent and insightful discussions, feedback, and ideas at every stage of my research that pushed me beyond my boundaries of critical thinking. Overall, her perspective on my research, constructive criticism, and advice has enabled me to complete my thesis. I could not have asked for a better co-supervisor for my Master of Science study.

Next, the completion of my graduate degree would not have been possible without the support of my fellow comrades at the Centre for Design of Advanced Materials (CDAM). I appreciate the collaboration and encouragement from my group mates Alex Yang and Kyle Mao. I'm extremely grateful to senior group members Cass Li, Kasra Rezasefat Balasbaneh, and Saman Sayahlatifi for taking the time to mentor me through my graduate studies. I would also like to thank our collaborators and industrial partners in this project for their guidance and feedback, including Dr. Dan Sameoto, Geneviève Toussaint, and Harry Templeman.

Finally and above all, I wish to offer my greatest thanks and special gratitude to my parents for their moral support, encouragement, and motivation. Without their long-lasting support, I would not have made it through my Master of Science degree.

This work is supported by Defence Research and Development Canada (DRDC), General Dynamics Land Systems–Canada, and NP Aerospace through NSERC Alliance project ALLRP 560447-2020. The views and conclusions contained in this document are those of the authors and should not be interpreted as representing the official policies, either expressed or implied, of General Dynamics, NP Aerospace, DRDC or the Government of Canada. The Government of Canada is authorized to reproduce and distribute reprints for Government purposes notwithstanding any copyright notation herein. This research was also enabled in part by support provided by Compute Ontario ([www.computeontario.ca/](http://www.computeontario.ca/)) and Compute Canada ([www.computecanada.ca](http://www.computecanada.ca)) via the Graham cluster. In addition, this research work was also funded by the Department of National Defence (DND) of Canada program Innovation for Defence Excellence and Security (IDEaS) under Project W7714-228051/001/SV1.herein.

# Table of Contents

<b>1</b>	<b>Introduction</b>	<b>1</b>
1.1	Motivation . . . . .	1
1.2	Thesis objectives . . . . .	2
1.3	Thesis goals . . . . .	3
1.4	Thesis contributions . . . . .	4
1.5	Thesis structure . . . . .	5
<b>2</b>	<b>Cohesive zone failure modeling of polymeric adhesives used in ceramic/metal armor</b>	<b>6</b>
2.1	Abstract . . . . .	7
2.2	Introduction . . . . .	7
2.2.1	Ceramic/metal armor . . . . .	7
2.2.2	Adhesive models . . . . .	9
2.3	Validation . . . . .	11
2.3.1	Cohesive zone adhesive model . . . . .	12
2.3.2	Ceramic/metal armor model . . . . .	15
2.4	Results and discussion . . . . .	26
2.4.1	Effect of adhesive thickness . . . . .	26
2.4.2	The role of defects on simulated armor performance . . . . .	30
2.4.3	A strain rate-dependent cohesive zone model . . . . .	33
2.5	Conclusions . . . . .	38

<b>3</b>	<b>Design of micro- and macro-scale polymeric metamaterial solutions for passive and active thermal camouflaging applications</b>	<b>40</b>
3.1	Abstract . . . . .	41
3.2	Introduction . . . . .	41
3.3	Results and discussion . . . . .	43
3.3.1	Polyethylene material model validation . . . . .	44
3.3.2	Macro-scale single-layered lenticular lens design . . . . .	45
3.3.3	Macro-scale sandwiched lenticular lens design . . . . .	47
3.3.4	Micro-scale post design . . . . .	49
3.4	Conclusion . . . . .	53
<b>4</b>	<b>Concluding remarks</b>	<b>54</b>
4.1	Implications . . . . .	54
4.2	Future work and recommendations . . . . .	55
	<b>Bibliography</b>	<b>58</b>
	<b>Appendix A: Appendices for Chapter 2</b>	<b>68</b>
A.1	Numerical methods . . . . .	68
A.1.1	Cohesive zone model . . . . .	68
A.1.2	Johnson-Holmquist II material model . . . . .	71
A.1.3	Johnson-Cook material model . . . . .	72
A.1.4	Cowper-Symonds strength model . . . . .	73
A.2	Numerical test set up of the double cantilever beam and end-notched flexure tests . . . . .	74
A.3	Element formulation and contact settings for the ceramic/metal armor model . . . . .	74

# List of Tables

2.1	Trilinear cohesive zone model parameters used to define the SikaForce <sup>TM6</sup> 7752-L60 polyurethane adhesive in LS-DYNA [26, 50, 51]. . . . .	14
2.2	Plastic kinematic model parameters used to define the aluminum adherends (AA6082 T651) in LS-DYNA [26, 52]. . . . .	15
2.3	Number of elements used for the medium mesh of the ceramic/metal armor model . . . . .	18
2.4	Johnson-Holmquist II parameters used to define the alumina ceramic tiles in LS-DYNA [60]. . . . .	21
2.5	Johnson-Cook parameters used to define the aluminum Al5083 H116 metal backing and steel 4340 projectile in LS-DYNA [1, 61]. . . . .	22
2.6	Mie-Gruneisen model equation of state parameters used to define the epoxy interlayer in LS-DYNA [1]. . . . .	23
2.7	Maximum effective strain at failure values for the erosion material model in LS-DYNA [1, 2] . . . . .	23
2.8	Depth of penetration results using coarse, medium, and fine element sizes. The absolute error difference is calculated relative to the results by Prakash et al. [2]. . . . .	25
2.9	Mode I and II critical energy release rates calculated for interlayer thicknesses of 0.50 mm to 1.50 mm. . . . .	27

2.10	Trilinear cohesive zone model parameters used to define the SikaForce <sup>TM6</sup> 7752-L60 polyurethane adhesive in LS-DYNA [26, 50, 51]. Strain rate dependency is considered by including rate-dependent terms of 3M <sup>TM</sup> Scotch-Weld <sup>TM</sup> AF 163-2OST structural epoxy adhesive [75]. . . . .	35
2.11	Adhesive damage area after impact for initial projectile velocities of 630 m/s, 830 m/s, and 1030 m/s with and without the strain rate terms implemented in the adhesive layer constitutive model. . . . .	37
2.12	Depth of penetration results for initial projectile velocities of 630 m/s, 830 m/s, and 1030 m/s with and without the strain rate terms implemented in the adhesive layer constitutive model. . . . .	38

# List of Figures

2.1	Experimental layout of the (a) double cantilever beam and (b) end-notched flexure tests used to numerically characterize strength and fracture of adhesives. A three-dimensional numerical model is constructed based on this layout (shown in Appendix A.2). . . . .	13
2.2	Comparison between experimentally and numerically obtained load-displacement curves for the (a) double cantilever beam and (b) end-notched flexure tests. Experimental data are obtained from results by Faneco et al. [26]. . . . .	16
2.3	Load-displacement results from the mesh sensitivity analysis for the (a) double cantilever beam and (b) end-notched flexure tests. . . . .	17
2.4	(a) Front view showing the dimensioned geometry of the 3D layered structure and projectile model and (b) a medium-sized mesh (0.7 mm element size) of the layered structure generated using HyperMesh [57].	19
2.5	Results from the mesh sensitivity analysis using the velocity-time history of the rear center node of the projectile for the coarse (1 mm), medium (0.7 mm), and fine (0.5 mm) mesh sizes. . . . .	24
2.6	Velocity-time history of the rear center node of the projectile as it penetrates through the armor structure (using the medium mesh). Comparison is made with simulation results by Prakash et al. [2] and Rashed et al. [1]. . . . .	25

2.7	(a) Velocity-time history of the rear center node of the projectile and (b) time to stop projectile for adhesive layer thicknesses between 0.50 mm and 1.50 mm. . . . .	28
2.8	Depth of projectile penetration (a) plotted against time and (b) into the metal backing layer for adhesive thicknesses between 0.50 mm and 1.50 mm. . . . .	29
2.9	Damage patterns on the alumina ceramic tile for adhesive thicknesses of: (a) 0.50 mm, (b) 0.75 mm, (c) 1.00 mm, (d) 1.25 mm, and (e) 1.50 mm. A cross-sectional view of the ceramic tile is provided below the isometric view for each of the thicknesses. . . . .	31
2.10	Air bubbles within the adhesive layer represented by deleted cohesive zone elements with gap ratios of: (a) 0.5%, (b) 2.5%, (c) 5%, and (d) 7.5%. . . . .	32
2.11	(a) Velocity-time history of the rear center node of the projectile (1.5%, 3.75%, and 6.25% porosities omitted for clarity) and (b) time to stop projectile for interlayer defect percentage ratios of 0% to 7.5%. . . . .	34
2.12	Depth of projectile penetration for interlayer defect percentage ratios of 0% to 7.5%. . . . .	36
2.13	Velocity-time history of the rear center node of the projectile for initial projectile velocities of 630 m/s, 830 m/s, and 1030 m/s with and without the strain rate-dependent model implemented for the adhesive layer constitutive model. . . . .	37
2.14	The damage region of the adhesive (a) with and (b) without implementing the strain rate-dependent terms into the cohesive zone model for the projectile travelling at an initial velocity of 830 m/s. . . . .	38

3.1	<p>COMSOL Multiphysics<sup>®</sup> model validation of a plain unstructured polyethylene sheet. (a) Unit cell geometry of a plain 10 μm thick polyethylene sheet with corresponding locations of boundary conditions. Additional Floquet periodic boundary conditions are used in the x- and y- directions. (b) Loss tangent-wavelength input plot to COMSOL Multiphysics<sup>®</sup> for a plain 10 μm thick polyethylene sheet. (c) Validated emissivity output for a 10 μm thick polyethylene film for the infrared spectrum (wavelengths of 5-16 μm). (d) Sensitivity of transmittivity results to polyethylene thickness, where the overall transmittivity decreases with increasing thickness in the infrared spectrum (wavelengths of 5-16 μm). . . . .</p>	46
3.2	<p>Simulating the macro-scale lenticular lens design in COMSOL Multiphysics<sup>®</sup>. (a) Global overall lenticular lens geometry. The inset image shows a unit cell geometry where <math>P = 195 \mu\text{m}</math>, <math>r = 100</math> to <math>750 \mu\text{m}</math>, <math>h = 78</math> to <math>6 \mu\text{m}</math>, and <math>t_p = 100 \mu\text{m}</math>. (b) Emissivity spectrum of the lenticular lens design with change of lens radius (<math>r = 100</math> to <math>750 \mu\text{m}</math> and <math>h = 78</math> to <math>6 \mu\text{m}</math>). (c) Emissivity/absorptivity and reflectivity spectra of the lenticular lens design (<math>r = 150 \mu\text{m}</math> and <math>h = 78 \mu\text{m}</math>) for varying angles of incidence (<math>\theta = 0^\circ</math> to <math>60^\circ</math>) suggesting a high dispersion of rays. (d) Spectral emissivity of the lenticular lens design (<math>r = 150 \mu\text{m}</math> and <math>h = 78 \mu\text{m}</math>) with an applied lateral strain in the x-direction (<math>\varepsilon_x = 0</math> to <math>0.03</math>). The inset image shows representative radii of the unit cell with applied lateral strain in the x-direction (not to scale). The macro-scale lenticular lens design allows for a high dispersion of rays while being stable under varying lens radii and strains. . . . .</p>	48

3.3 Simulating the macro-scale lenticular lens sandwiched structure design in COMSOL Multiphysics<sup>®</sup>. (a) Global overall sandwiched lenticular lens geometry (lens facing inwards) with air between the sheets. The inset image shows a unit cell geometry where  $t_{air} = 85$  to  $175 \mu\text{m}$ ,  $r = 100$  to  $750 \mu\text{m}$ ,  $h = 78$  to  $6 \mu\text{m}$ , and  $t_p = 100 \mu\text{m}$ . The configuration with the lens facing outwards is also investigated. Emissivity spectrum of the lenticular lens sandwiched structure with change of: (b) air gap between the lenticular lens sheets ( $t_{air} = 85$  to  $175 \mu\text{m}$ ); and (c) change of lens radius ( $r = 100$  to  $750 \mu\text{m}$  and  $h = 78$  to  $6 \mu\text{m}$ ) for both lens facing inwards and outwards configurations. The lens facing outwards design has a lower emissivity within the mid-infrared wavelengths for all lens radii and air gaps. (d) Emissivity/absorptivity and reflectivity spectra of the lenticular lens sandwiched structure (lens facing inwards,  $r = 150 \mu\text{m}$  and  $h = 78 \mu\text{m}$ ) for varying angles of incidence ( $\theta = 0^\circ$  to  $60^\circ$ ). Similar trends are observed for the lens facing outwards configuration. A high dispersion of rays is evident from the shift of optical properties due to varying angles of incidence of the IR light, while demonstrating emissive stability under the various geometrical configurations. . . . . 50

3.4 Simulating the micro-scale posts design in COMSOL Multiphysics®.

(a) Global overall post geometry. The inset image shows a unit cell geometry where  $a = 1$  to  $9\ \mu\text{m}$ ,  $b = 1$  to  $9\ \mu\text{m}$ ,  $h = 1$  to  $9\ \mu\text{m}$ , and  $t_p = 10\ \mu\text{m}$ . (b) Emissivity spectrum of the post lens design with change in post size and spacing where  $a = 1$  to  $9\ \mu\text{m}$ ,  $b = 1$  to  $9\ \mu\text{m}$ , and  $h = 1$  to  $9\ \mu\text{m}$ . (c) Emissivity/absorptivity and reflectivity spectra of the post configuration ( $a = 9\ \mu\text{m}$  and  $b = 5\ \mu\text{m}$ ) for varying angles of incidence ( $\theta = 0^\circ$  to  $60^\circ$ ). (d) Spectral emissivity of the post configuration ( $a = 9\ \mu\text{m}$  and  $b = 5\ \mu\text{m}$ ) with an applied lateral strain in the x-direction ( $\varepsilon_x = 0$  to  $0.03$ ). Micro-sized posts allow for highly-customizable solutions for thermal radiation control. . . . . 52

A.1 Trilinear traction separation law used in the cohesive mixed-mode elastoplastic rate material model in LS-DYNA [46]. . . . . 69

A.2 Isometric view of the mesh for (a) the double cantilever beam and (b) the end-notched flexure test setups with an element size of 1 mm based on the experimental work performed by Faneco et al. [26]. . . . . 75

A.3 Hinge placement locations on (a) the double cantilever beam and (b) the end-notched flexure test setups based on the experimental work performed by Faneco et al. [26]. . . . . 76

# List of Symbols

## General material properties

$\nu$	Poisson's ratio
$\rho$	Density
$E$	Young's modulus
$G$	Shear modulus
$S$	Shear strength
$T$	Yield strength

## Geometrical and load symbols

$\delta$	Separation displacement
$a_0$	Initial crack length
$L_{DCB}$	Beam length
$L_{ENF}$	Midspan length
$P$	Applied load
$p$	Pressure
$t_A$	Adhesive thickness
$t_P$	Adherend thickness

## Subscripts

$S$	Shear stress
-----	--------------

$T$  Tensile stress

### **Cohesive zone model parameters**

$\dot{\epsilon}_S$  Equivalent strain rate term of shear stress

$\dot{\epsilon}_T$  Equivalent strain rate term of yield stress

$\dot{\epsilon}_{Gi}$  Equivalent strain rate term of mode  $i$  critical energy release rate ( $i=I,II$ )

$\gamma_i$  Mode  $i$  critical energy release rate coefficient ( $i=I,II$ )

$\tau_i$  Mode  $i$  critical energy release rate exponent ( $i=I,II$ )

$f_{Gi}$  Mode  $i$  plastic to total area ratio ( $i=I,II$ )

$G_{iC}$  Mode  $i$  critical energy release rate ( $i=I,II$ )

$G_{ij}$  Lower ( $j=0$ ) and upper ( $j=\infty$ ) bound of mode  $i$  critical energy release rate ( $i=I,II$ )

$S_j$  Lower bound ( $j=0$ ) and upper bound ( $j=1$ ) of shear stress

$T_j$  Lower bound ( $j=0$ ) and upper bound ( $j=1$ ) of yield stress

### **Johnson-Holmquist II model parameters**

$\beta$  Bulking constant

$\dot{\epsilon}_{JH2}$  Johnson-Holmquist II reference strain rate

$\mu_{JH2}$  Johnson-Holmquist II excess compression term

$a_{JH2}$  Johnson-Holmquist II intact strength constant

$b_{JH2}$  Johnson-Holmquist II fractured strength constant

$c_{JH2}$  Johnson-Holmquist II strain rate constant

$d_1$  Damage constant

$d_2$  Damage exponent

$FS$  Failure strain

*HEL* Hugoniot elastic limit

$k_i$  Bulk modulus ( $i=1$ );  $i$ th pressure coefficient ( $i=2,3$ )

$m_{\text{JH2}}$  Johnson-Holmquist II fractured strength exponent

$n_{\text{JH2}}$  Johnson-Holmquist II intact strength component

$p^*$  Maximum tensile strength

$p_{\text{HEL}}$  Pressure at HEL

$SF_{\text{MAX}}$  Maximum fracture strength ratio

### **Johnson-Cook model parameters**

$\dot{\epsilon}_{\text{JC}}$  Johnson-Cook reference strain rate

$\mu_{\text{JC}}$  Johnson-Cook excess compression term

$b_{\text{JC}}$  Johnson-Cook hardening constant

$C_1$  Bulk modulus for the linear equation of state

$c_{\text{JC}}$  Johnson-Cook strain rate constant

$C_P$  Specific heat

$D_i$  Failure parameter  $i$  ( $i=1,2,3,4,5$ )

$m_{\text{JC}}$  Johnson-Cook thermal softening exponent

$n_{\text{JC}}$  Johnson-Cook hardening exponent

$T_{\text{melt}}$  Melting temperature

$T_{\text{room}}$  Room temperature

### **Mie-Gruneisen model parameters**

$\gamma_0$  Gruneisen gamma

$a$  First order volume correction to Gruneisen gamma

$C$  Intercept to the cubic shock-velocity versus particle velocity curve

$S_{\text{MG},i}$  Coefficient  $i$  to the cubic shock-velocity versus particle velocity curve ( $i=1,2,3$ )

# Abbreviations & Acronyms

**2D** Two-dimensional.

**3D** Three-dimensional.

**CZM** Cohesive zone modelling.

**DCB** Double cantilever beam.

**DOP** Depth of penetration.

**ENF** End-notched flexure.

**HEL** Hugoniot Elastic Limit.

**IR** Infrared.

**JC** Johnson-Cook.

**JH2** Johnson-Holmquist II.

**MIR** Mid-infrared.

**TAST** Thick adherend shear test.

**TCZM** Trilinear cohesive zone model.

**TSL** Traction separation law.

# Chapter 1

## Introduction

### 1.1 Motivation

Hybrid armor systems are frequently used in armored vehicles to protect against high-level ballistic threats. These systems commonly comprise of ceramic tiles bonded to a metal backing by using an adhesive interlayer [1–5]. The ceramic tiles assist in eroding/blunting [6] or shattering the projectile tip [7], and reducing its kinetic energy because of its high hardness and compressive strength [8]. The metal backing further absorbs the energy from the impact due to its ductile properties, which assist in slowing down and stopping the projectile, and preventing it from penetrating the layered structure [6]. The adhesive interlayer bonds the layers together, and also controls the stress and shock waves propagating through the layers which are known to cause premature failure in the ceramic tiles through reflected tensile waves [9]. In addition, the interlayer keeps the damaged ceramic plate bonded to the metal backing after a high-velocity impact event [10], allowing protection from multi-hit capabilities. To further our understanding of the influence that the interlayer has on the performance of armor systems, this thesis implements and explores adhesive modelling techniques to simulate dynamic ballistic events on hybrid armor systems.

In addition to developing armor against kinetic threats, research in the literature has also been done to develop coatings [11], metamaterials [12, 13], and passive [14] and active [15, 16] systems for infrared (IR) camouflage. Recent research in materials

development for IR camouflage have primarily focused on manufacturing multilayered metamaterials with microstructures [14, 16, 17] and micro-scaled structures consisting of nanowires/nanotubes [18–20]. The bulk of the research on this topic has involved manufacturing lab-scale coupons of various layered configurations (e.g., metallic disks on a multilayered structure [12, 13, 17, 21] and composites consisting of metals/metalloids and ceramics [11, 14, 22]), with few studies incorporating numerical simulation tools in design [13, 21, 23–25]. For these numerical studies, efforts have been focused on experimental validation and guiding design decisions to optimize thermal signature management capabilities. However, these models are limited in their ability to: (1) inform material mechanisms under the IR regime, (2) provide a measure of scattering from IR light interactions with the composite structure, (3) perform numerical multiphysics techniques to develop models capable of simulating strain modulation for active IR camouflage, (4) utilize macro-scaled geometries (e.g., lenticular lenses) to enhance optical scattering for passive IR camouflage, and (5) utilize optical properties (such as reflectivity, transmittivity, absorptivity, and emissivity) as performance indicators of IR camouflage. This thesis addresses the above gaps by utilizing multiphysics modelling techniques for composite armor that considers IR camouflage capabilities.

## 1.2 Thesis objectives

The objective of this thesis is to develop: (1) a finite element model in LS-DYNA to simulate the dynamic failure of adhesives (e.g., damage accumulation, fracture processes, and microstructural effects) used in hybrid armor systems for land vehicles under ballistic impact, and (2) an optical model in COMSOL Multiphysics to simulate the interaction (absorptivity and emissivity) between materials with micro-features (e.g., polyethylene (PE)) and IR light.

In objective (1), this thesis utilizes a strain-rate-dependent cohesive zone modelling approach in the explicit nonlinear finite element software, LS-DYNA, to model the impact and failure behavior of the polyurethane adhesive material within a larger

composite armor system. Specifically, this thesis investigates the effects of manufacturing defects (in the form of air bubbles), strain rate, and thickness of the adhesive layer towards meeting its objective. This thesis is important because: (1) limited studies have considered the effects that the adhesive layer has on the performance of armor systems, (2) this study provides novel insights to modelling adhesive defects and the effects they have on armor performance, and (3) the research bridges the gap in the literature by exploring the relationship between change in adhesive thicknesses and critical energy release rates with relation to armor performance.

To meet objective (2), this thesis simulates polymeric metamaterials for IR camouflage applications using COMSOL Multiphysics software. Specifically, the radio frequency (RF) module is used to simulate the interaction between IR light and polyethylene to evaluate the resulting absorptivity/emissivity, reflectivity, scattering, and transmittivity values. These metrics define the optical properties of a material, and can be tuned to improve the IR camouflage performance by decreasing emissivity and increasing scattering of IR radiation. This thesis component is important because: (1) the proposed model aids in guiding design choices (e.g., material selection and overall layer configurations) and geometries (e.g., shapes and sizes of surface features, and thickness of sheets) of systems used for tunable surface emissivity to achieve IR camouflage and (2) it informs material mechanisms to improve thermal radiating performance.

### **1.3 Thesis goals**

The goals of this thesis are summarized as follows:

1. Develop, validate with literature data [26], and implement a trilinear cohesive zone polyurethane adhesive model [27] into a validated multi-scale model to simulate damage accumulation and interface failure that occur through high-velocity ballistic impact.

2. Exercise the system-scale armor model to explore the effects of the following parameters on armor performance: (1) the adhesive thickness, (2) strain rate, and (3) manufacturing defects (through simulated air bubbles) within the adhesive layer.
3. Develop, validate, and implement a numerical multiphysics optical model using unit cell configurations for IR camouflage applications. Here, the polyethylene material model is validated with literature data [28] and is exercised through a parametric study to inform micro- and macro-scale design configurations (e.g., posts, lenticular lenses, and sandwiched structures) for needed to improve camouflage performance (through passive and active methods of actuation).

## 1.4 Thesis contributions

The contributions of this thesis are summarized as follows:

1. Made novel contributions in implementing a rate-dependent energy-based tri-linear cohesive zone fracture modelling approach to simulate adhesives used in armor systems. To date, no studies have utilized this approach to numerically characterize strength and fracture of adhesives bonding ceramic tiles to a metal backing layer in armor systems.
2. Provided a novel modelling technique and insights in simulating defects (trapped air bubbles) within the adhesive layer through the use of randomly deleted cohesive zone elements, and how these defects hinder armor performance.
3. Made valued contributions in understanding the factors that govern the impact performance of armor systems. Specifically, the effects of fracture formations, thickness, manufacturing defects, geometry, and material properties of the adhesive layer are explored.

4. Made novel contributions in designing thermal radiation solutions through passively and actively modulated tunable IR emitting surfaces (e.g., lenticular lenses, posts, and sandwiched structures) by modelling the interaction between IR radiation and polyethylene.

## 1.5 Thesis structure

This thesis is organized as follows:

- Chapter 1 introduces the motivation for developing (1) an adhesive model undergoing ballistic impact and (2) a multiphysics optical model for thermal signature management. This chapter further outlines the thesis objectives, thesis goals, contributions, and thesis structure.
- Chapter 2 details a study focused on developing and validating a trilinear cohesive zone model and a system-scale armor model. Here, the effects the adhesive thickness, defects within the interlayer, and strain rate have on armor performance are explored. This study, titled “Cohesive Zone Failure Modelling of Polymeric Adhesives used in Ceramic/Metal Armor”, has been published in *International Journal of Impact Engineering* [29].
- Chapter 3 details a study on the development of an optical model of polyethylene in posts and lenticular lens configurations for IR camouflage applications. Validation and design choices to optimize performance are discussed. This study, titled “Design of Micro- and Macro-scale Polymeric Metamaterial Solutions for Passive and Active Thermal Camouflaging Applications”, has been submitted to *Advanced Physics Research* in August 2022.
- Chapter 4 summarizes the outcomes and implications of this research and outlines directions for future work.

## Chapter 2

# Cohesive zone failure modeling of polymeric adhesives used in ceramic/metal armor

Part of this Chapter published as **Harshil Pisavadia**; Geneviève Toussaint; Patricia Dolez, and James Hogan. *Cohesive Zone Failure Modeling of Polymeric Adhesives used in Ceramic/Metal Armor*. International Journal of Impact Engineering. (2022)

---

Author	Contributions
Harshil Pisavadia	Conceptualization, Methodology, Software, Validation, Formal analysis, Writing - Original Draft, Visualization
Geneviève Toussaint	Writing - Review & Editing
Patricia Dolez	Writing - Review & Editing, Supervision
James Hogan	Principal investigator, Conceptualization, Writing - Review & Editing, Supervision

---

## 2.1 Abstract

In this paper, a trilinear cohesive zone modeling approach available in the explicit nonlinear finite element software LS-DYNA is used to model the dynamic impact failure of an adhesive layer. This approach is an improvement over simpler cohesive zone models presented in the literature. The model is validated for the SikaForce<sup>TM6</sup> 7752-L60 polyurethane adhesive using force-displacement curves of double cantilever beam and end-notched flexure tests extracted from the literature. The trilinear cohesive zone model was then implemented to simulate the behavior of the adhesive bonding a ceramic alumina tile to an aluminium backing. Simulations were performed to explore the effect of the adhesive layer thickness, manufacturing defects (air bubbles simulated through deleted elements), and strain rates. It was found that: (1) a thicker adhesive layer decreased the ceramic/metal armor performance for a single hit, but resulted in a reduction of the damage area of the top ceramic tile in simulations; (2) an increase in the amount of defects resulted in greater depth of penetration and increased delays to stop the projectile, resulting in a reduction of simulated armor performance; and (3) including strain rate effects in the model resulted in predictions of a reduced depth of penetration and an increase in the damage region of the interlayer after the impact event for all of the simulated impact velocities, thereby predicting a decreased performance for multi-hit impact conditions of the armor system.

## 2.2 Introduction

### 2.2.1 Ceramic/metal armor

The performance of armor systems can be improved by better designing the adhesive layer used to bond the ceramic tiles to the metal backing layer in the armor system [30]. Here, the adhesive layer plays a critical role during impact in controlling wave propagation that leads to damage accumulation within the armor structure, ultimately affecting armor performance [31]. In the open literature, some experimental

and numerical studies have investigated the effects adhesives have on the performance of armor systems. For example, Zaera et al. [10] explored the effects that different thicknesses (0.5 mm to 1.5 mm) of polyurethane and epoxy resin adhesives have on armor efficiency. It was concluded that thicker adhesives caused more damage to the ceramic tile, and this damage was due to the ceramic being unsupported by the backing for a greater period of time; however, a thicker layer of adhesives reduced the degree of fragmentation of the adjacent tiles. In another study, López-Puente et al. [32] identified three different factors related to the adhesive thickness performance that have an influence on the armor efficiency: shear stress, ceramic spalling, and energy absorption. They concluded that an epoxy adhesive thickness of 0.3 mm was optimum to (1) minimize adhesive shear stress, (2) minimize ceramic spalling, and (3) increase the energy absorption mechanism of the metal backing for armors consisting of an alumina ceramic plate bonded to an aluminum metal backing. In a separate study, Shen et al. [4] performed experimental and numerical studies to investigate the effect of the adhesive layer thicknesses (0.2 mm to 3.0 mm) on the ceramic/metal armor. It was concluded that the optimum adhesive layer thickness during multi-hit impact conditions was 2 mm. In their studies, Prakash et al. [2] and Arslan et al. [33] performed numerical simulations using a Cowper-Symonds strength model and an elastic-plastic material model to model their epoxy adhesive layer within an armor system. Prakash et al. [2] found that a thicker adhesive also led to greater plastic deformation in the metal backing layer, and Arslan et al. [33] concluded that the residual velocity of the projectile was found to increase with increasing adhesive thickness. Therefore, both of these studies found that increasing the adhesive thicknesses decreases the armor performance. In a separate study, Seifert et al. [3] performed experimental tests to investigate the effects of the adhesive stiffness on the armor performance and they found that a higher fracture strain led to greater deformation in the backing plate and adhesion strength was found to be dependent on loading rates. Overall, studies have shown that a thin adhesive layer has better performance

against a single shot, however, during multi-hit impact conditions, a thicker adhesive layer reduce the degree of fragmentation and damage to adjacent tiles. Further, when studying the effect of adhesive thickness on the overall armor performance, the above numerical studies did not take into consideration the functional relationships between the adhesive material and its geometrical properties [34, 35], as we do in the current study.

### **2.2.2 Adhesive models**

The cohesive zone modeling (CZM) approach is a widely used technique to model adhesive joints [4, 36–40] and interfaces where interlaminar damage (e.g., delamination) occurs [41–43]. However, limited studies have utilized this energy-based approach to numerically characterize strength and fracture of adhesives used in armor applications [4, 36, 44]. In these examples, the bilinear CZM approach was used by Bürger et al. [36] and Goda and Girardot [44] to model the adhesive layer of ceramic/fiber reinforced composite armors and by Shen et al. [4] to model the adhesive layer bonding ceramics to a metal backing. These studies did not consider plasticity in the adhesive material as they used the bilinear approach for the traction separation law. Therefore, we improve upon this in the current study by considering plastic behavior during separation at failure through the trilinear (or trapezoidal) traction separation law. Using this new formulation, the dynamic failure of adhesives is more accurately predicted [27]. To date, no studies have considered using the trilinear cohesive zone model (TCZM) to represent the adhesive layer bonding the ceramic tiles to a metal backing layer. In another study, Jia et al. [45] studied the effects that high strain rates have on polyurethane adhesives with validations using the thick adherend shear test (TAST), the double cantilever beam (DCB) test, and the end-notched flexure (ENF) test. It was concluded that the adhesive can be simulated using a strain rate-dependent CZM approach under various impact conditions, and this will be the approach taken in this paper. Building on these, this present investigation expands

the research of previous studies by considering functional dependency of crucial adhesive material properties (i.e., modes I and II critical energy release rates) due to changes in thickness while using a trapezoidal traction separation law to consider plasticity in the cohesive elements. In addition, no studies have yet considered the effect of realistic manufacturing problems such as trapped air within the adhesive layer in composite armor structures, as we do here. This is an important aspect to consider since the performance of these systems can be heavily affected by challenges in quality control (i.e., manufacturing defects).

Finally, the damage resulting from ballistic impact on composite structures consists of complex failure mechanisms. Specifically, the damage response needs to be accurately simulated within each of the composite layers (including the front ceramic tile, metal backing layer, and the adhesive used to bond the system together) and the projectile, including the interaction between each of these subsystems [44]. Therefore, both interlaminar and intralaminar damage are important to consider to accurately predict damage under loading when modeling interfaces in composite structures [42, 43]. Here, Maziz et al. [42] and Maziz et al. [43] evaluated intralaminar damage (e.g., matrix cracks and fiber failures) of pressurized hybrid pipe structures using the Hashin criteria, and interlaminar damage (e.g., ply delamination) was modeled using the bilinear cohesive law.

Motivated by these past investigations, this study applies a mixed-mode trilinear cohesive zone damage model to simulate impact-induced fractures in polymeric adhesives to be used in ceramic/metallic armor of vehicles. In the current work, the TCZM was implemented in the explicit nonlinear finite element software, LS-DYNA code version R11.1.0 [46]. This new approach improves the modeling of system-scale armor [1, 2] by including damage [47], plasticity [48], and rate-dependent terms [27], and also enables simulating initiation and cracks growth within the adhesive layer [36]. These important considerations lead to improved layers delamination modeling of the layers in the structure which has been shown to be critical in the overall perfor-

mance of armor systems [4]. The TCZM implementation for the adhesive is validated first by comparing numerical results to mechanical test results obtained for the double cantilever beam and end-notched flexure tests [26], followed by a comparison with ballistic simulation data extracted from the literature [1, 2]. Once validated, simulations are then performed to explore how performance is affected by the adhesive thickness and strain rates. For the first time in the literature, this work attempts to provide a better understanding of: (1) the interplay between the critical energy release rate and change in adhesive thicknesses, (2) the effects of manufacturing defects such as air bubbles trapped within the adhesive layer (defects in the form of deleted cohesive zone elements) on performance, and (3) the role of strain rate-dependent parameters of the adhesive material on the ballistic response of ceramic/metal armors. These new understandings are achieved through incorporating an elastic-plastic trilinear cohesive zone method that improves upon other studies in the literature [4, 44]. In addition, we also consider more realistic simulation setups: (1) uncertainty from experiments is considered in the cohesive zone model due to variability in both the experimental procedures and materials, (2) depth of penetration is analyzed over the entire impact timeframe to better visualize the times in which the projectile penetrates each of the individual layers of the armor structure, and (3) variabilities of cohesive parameters are considered by varying adhesive thicknesses.

## 2.3 Validation

This section discusses the validation of both the adhesive and the ceramic/metal armor models. Experimental data of the SikaForce<sup>TM6</sup> 7752-L60 polyurethane adhesive from Faneco et al. [26] is used to validate the adhesive model. Numerical data from Prakash et al. [2] and Rashed et al. [1] are used to validate the ballistic response of a projectile impacting a ceramic/metal armor system.

### 2.3.1 Cohesive zone adhesive model

The CZM parameters for the SikaForce<sup>TM6</sup> 7752-L60 polyurethane adhesive are obtained from experimental results provided by Faneco et al. [26]. Tensile and shear mechanical properties are obtained from bulk tensile and thick adherend shear test (TAST) results, respectively. The tensile properties include the Young’s modulus,  $E$  (Pa), and the yield strength,  $T$  (Pa). The shear properties include the shear modulus,  $G$  (Pa), and the shear strength,  $S$  (Pa). The tensile and shear strain energy release rate parameters,  $G_{IC}$  (N/m) and  $G_{IIC}$  (N/m), are obtained from the double cantilever beam test (DCB) (mode I) and the end-notched flexure test (ENF) (mode II), respectively. These two parameters are the most important parameters in CZM as they govern the onset of adhesive failure [49]. Details of the TCZM technique used in the simulations are detailed in Appendix A.1.

The experimental layouts of DCB and ENF tests performed by Faneco et al. [26] are presented in Fig. 2.1, where the top and bottom bars represent the adherends and the shaded region between the bars represent the adhesive layer. In both Fig. 2.1a and 2.1b,  $P$  (N) is the applied load,  $\delta$  (m) is the separation displacement,  $a_0$  (m) is the initial crack length,  $t_A$  (m) is the adhesive thickness, and  $t_P$  (m) is the adherend thickness.  $L_{DCB}$  (m) and  $L_{ENF}$  (m) are the beam length and the midspan length for the DCB and ENF test specimens, respectively. More details of the experimental setup of the DCB and ENF tests can be found in the study by Faneco et al. [26]. Aluminum is used as the upper and lower adherends for the DCB and ENF tests based on the setup of Faneco et al. [26]. The SikaForce<sup>TM6</sup> 7752-L60 polyurethane is used as the representative adhesive layer material in our current models. An adhesive thickness of 1 mm is used for the DCB and ENF tests following Faneco et al. [26]. Note that it is very important to consider the placement of the hinges and applied load when numerically simulating these tests as these influence the stiffness of the entire setup, and so great care is given in these simulations to match the setups from

Faneco et al. [26]. A schematic of the numerical model replicating the experimental test setup from Faneco et al. [26] is provided in Appendix A.2 Fig. A.2. Appendix A.2 further details the element formulation and contact definitions used in these simulations.

These model parameters determined from the experiments are summarized in Table 2.1, where strain rate effects are not included for these quasi-static loading conditions. The density of the adhesive is obtained from the material datasheet provided by the adhesive manufacturer [50]. When conducting these simulations, experimental and material variabilities are accounted for by using the minimum and maximum values of all the mechanical properties to one standard deviation of the mean as measured by Faneco et al. [26].

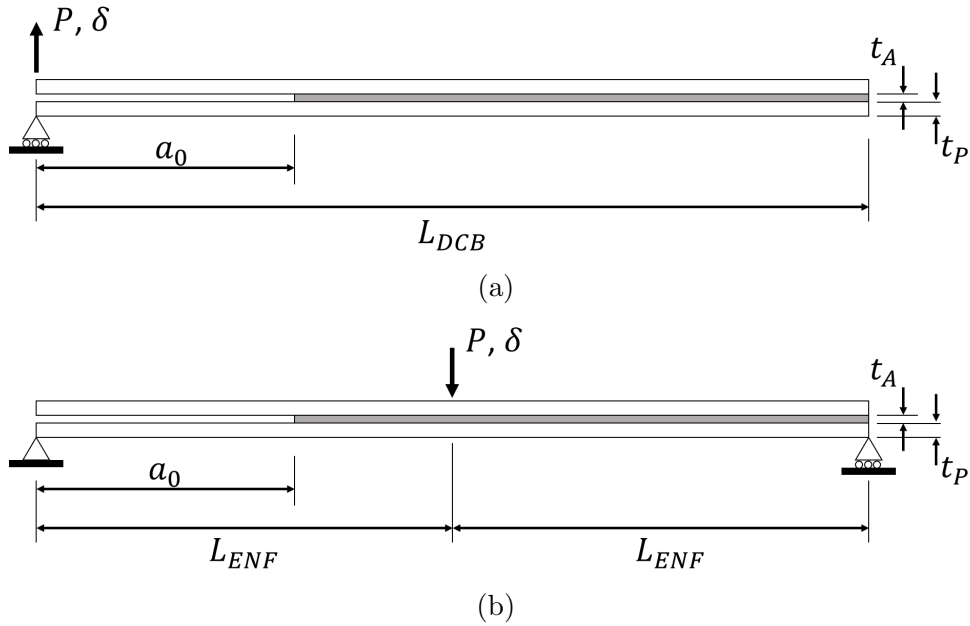


Figure 2.1: Experimental layout of the (a) double cantilever beam and (b) end-notched flexure tests used to numerically characterize strength and fracture of adhesives. A three-dimensional numerical model is constructed based on this layout (shown in Appendix A.2).

A plastic kinematic model (`*MAT_PLASTIC_KINEMATIC`) is implemented for the aluminum (AA6082 T651) adherends. This model is chosen since it considers isotropic and kinematic hardening plasticity behaviors [53]. Material parameters for the alu-

Table 2.1: Trilinear cohesive zone model parameters used to define the SikaForce<sup>TM6</sup> 7752-L60 polyurethane adhesive in LS-DYNA [26, 50, 51].

Model Parameters	Value	Units
Density ( $\rho$ ) [50]	1600	kg/m <sup>3</sup>
Young's modulus ( $E$ ) [26]	$4.93(\pm 0.90) \times 10^8$	Pa
Shear modulus ( $G$ ) [26]	$1.88(\pm 0.16) \times 10^8$	Pa
Yield strength ( $T$ ) [26]	$3.24(\pm 0.48) \times 10^6$	Pa
Shear strength ( $S$ ) [26]	$5.16(\pm 1.14) \times 10^6$	Pa
Lower bound of mode I critical energy release rate ( $G_{I0}$ ) [26]	$2.36(\pm 0.17) \times 10^3$	N/m
Lower bound of mode II critical energy release rate ( $G_{II0}$ ) [26]	$5.41(\pm 0.47) \times 10^3$	N/m
Mode I plastic to total area ratio ( $f_{G1}$ ) [51]	0.13	-
Mode II plastic to total area ratio ( $f_{G2}$ ) [51]	0.9	-

minimum adhesion are obtained from Faneco et al. [26] and the Poisson's ratio is obtained from Shengze et al. [52]. These parameters are summarized in Table 2.2.

To perform model validation, three-dimensional models of the DCB and ENF tests are set up in LS-DYNA. These DCB and ENF tests have been used to acquire model parameters for adhesives used in many applications and studies [36, 41, 49, 54, 55]. In this current study, model validation includes comparisons between experimentally obtained and simulated load-displacement ( $P - \delta$ ) curves from the DCB and ENF tests, as well as considerations for mesh sensitivity of these results (shown later in Fig. 2.3).

Comparisons between the experimentally obtained DCB and ENF  $P - \delta$  curves from Faneco et al. [26] and simulation results are presented in Fig. 2.2 using an element size of 1 mm. The simulated data consider the variability in material properties of the adhesive where the upper and lower bounds of the simulated data are obtained from using the maximum and minimum mechanical and fracture properties of the adhesive

Table 2.2: Plastic kinematic model parameters used to define the aluminum adherends (AA6082 T651) in LS-DYNA [26, 52].

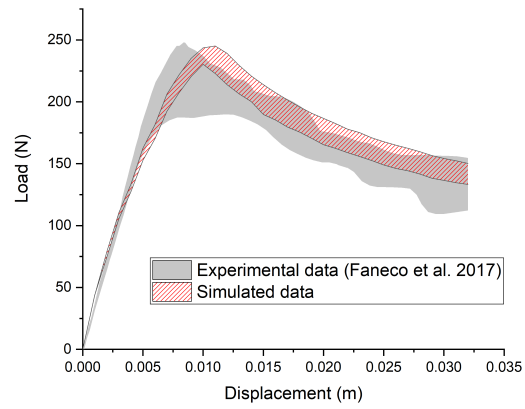
Model Parameters	Value	Units
Density ( $\rho$ )	$2.79 \times 10^3$	kg/m <sup>3</sup>
Young’s modulus ( $E$ )	$7.01(\pm 0.08) \times 10^{10}$	Pa
Poisson’s ratio ( $\nu$ )	0.269	-
Yield strength ( $T$ )	$2.62(\pm 0.08) \times 10^8$	Pa

within one standard deviation as provided by Faneco et al. [26]. The bounded region of the simulated data from Fig. 2.2 also considers the uncertainty of the hinge placement locations in the experimental setup performed by Faneco et al. [26]. In total, 14 simulations were performed each for the DCB and ENF test configurations. For both the DCB and ENF configurations in Fig. 2.2, the initial elastic region, peak load, and damage initiation to failure are in reasonable agreement to the experimental data. Specifically, the absolute peak error difference is 1.1% for the DCB test and 5.3% for the ENF test. For all other conditions, both the experimental and simulated curves overlap well, and thus our implementation of the adhesive model is considered validated for simple mechanical testing.

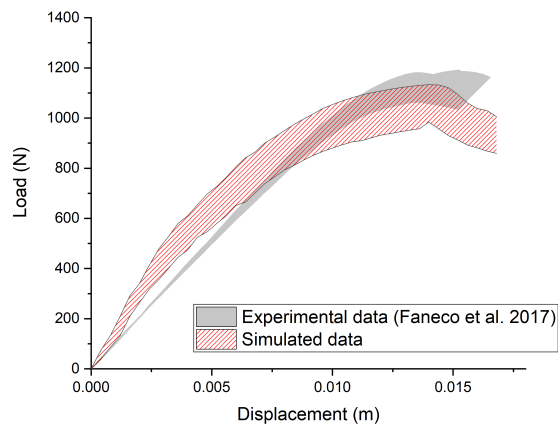
Mesh sensitivity analysis is also performed by generating the  $P - \delta$  curves using: (1) coarse: 2 mm; (2) medium: 1 mm; and (3) fine: 0.5 mm element sizes. These sizes are informed by the common element size selection from the literature [40, 54, 56]. The results from the mesh study are presented in Fig. 2.3 for both the DCB and ENF tests. From Fig. 2.3, the results show convergence for the 0.5 mm and 1 mm element size for both type of tests.

### 2.3.2 Ceramic/metal armor model

A three-dimensional (3D) armor model consisting of 99.5% purity alumina ceramic tile bonded with an epoxy layer to an aluminum Al5083 H116 backing is created to

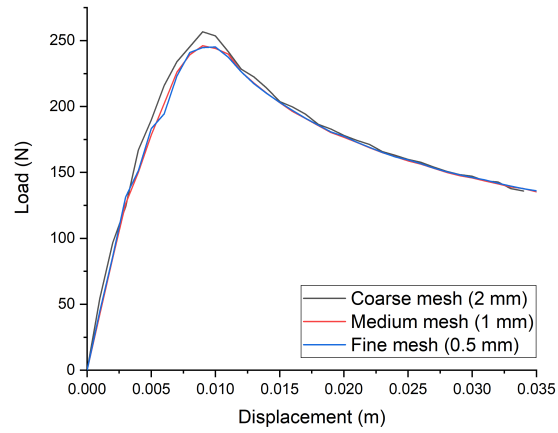


(a)

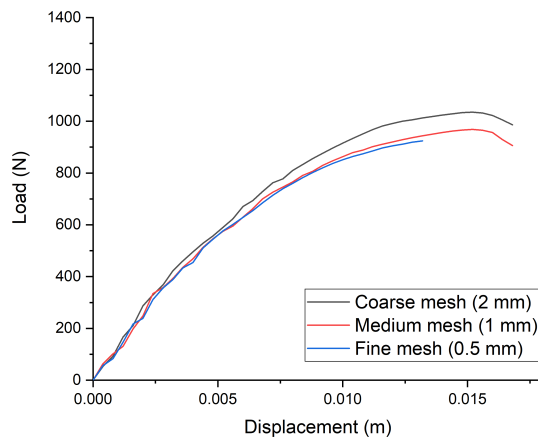


(b)

Figure 2.2: Comparison between experimentally and numerically obtained load-displacement curves for the (a) double cantilever beam and (b) end-notched flexure tests. Experimental data are obtained from results by Faneco et al. [26].



(a)



(b)

Figure 2.3: Load-displacement results from the mesh sensitivity analysis for the (a) double cantilever beam and (b) end-notched flexure tests.

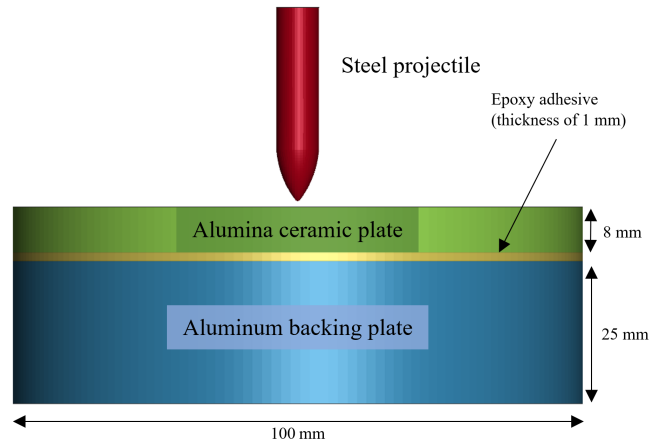
Table 2.3: Number of elements used for the medium mesh of the ceramic/metal armor model

Part	Number of elements
Projectile	32300
Ceramic front layer	285824
Adhesive interlayer	25984
Metal backing layer	935424

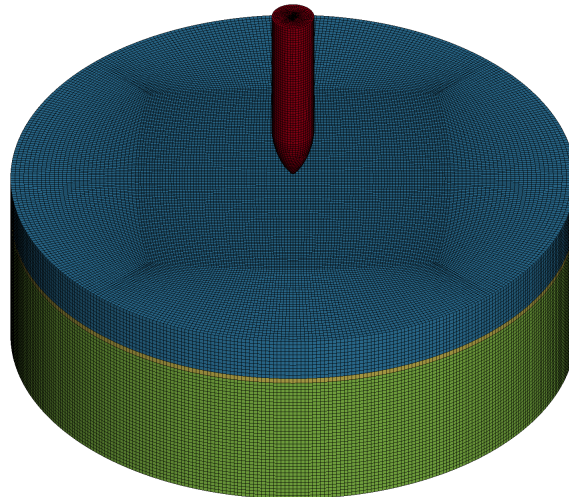
represent the two-dimensional (2D) model given by Prakash et al. [2] and Rashed et al. [1]. The 3D geometry in this investigation is chosen over a 2D geometry as used by Prakash et al. [2] and Rashed et al. [1] since 3D cohesive elements are implemented later in this study. The 3D model in the current investigation simulates a 7.62 mm projectile made of steel 4340 (length of 34 mm and mass of 10.3 g) impacting a ceramic/metal layered structure at 830 m/s. A schematic of this model with its dimensions and the medium-sized mesh is presented in Fig. 2.4. The number of elements for each of the model constituents is provided in Table 2.3. The outside cylindrical face of the model is fully fixed to simulate clamping as was done by Prakash et al. [2] and Rashed et al. [1]. The model was validated by comparing depth of penetration (DOP) and the projectile velocity-time history provided in published papers [1, 2]. Once the model was validated, the epoxy layer was replaced by the SikaForce<sup>TM6</sup> 7752-L60 polyurethane adhesive layer. These results are presented later in this paper.

### Constitutive models

The components and constitutive models used to simulate a 4340 steel 7.62 mm projectile impacting a composite armor consisting of 99.5% purity alumina ceramic tile bonded to an aluminum Al5083 H116 metal backing with a SikaForce<sup>TM6</sup> 7752-L60 [50] polyurethane adhesive layer are provided in Appendix A.1. The Johnson-Cook



(a)



(b)

Figure 2.4: (a) Front view showing the dimensioned geometry of the 3D layered structure and projectile model and (b) a medium-sized mesh (0.7 mm element size) of the layered structure generated using HyperMesh [57].

(JC) [58] material model is used to model the projectile and metal backing, the Johnson-Holmquist II (JH2) [59] material model is used to model the ceramic tile, and the trilinear cohesive zone modeling (TCZM) technique [27] is used to simulate the adhesive layer.

The JH2 material model parameters for 99.5% alumina are obtained from Cronin et al. [60] and are summarized in Table 2.4. The JC material model parameters for aluminum and steel are obtained from Rashed et al. [1] and are summarized in Table 2.5. The yield stress parameter for the aluminum JC model is modified based on the value from Flores-Johnson et al. [61]. This value corresponds to the yield stress of the aluminum AA7075-T651 alloy tuned for a 3D impact simulation. The epoxy material is modeled using a Cowper-Symonds strength model following [1, 2] and neglecting effects of strain rate. Further details of the strength model are provided in Appendix A.1. The parameters used to define the epoxy material model are obtained from Rashed et al. [1] and are summarized in Table 2.6.

To discard the highly distorted regions of the system during impact, an erosion criterion for each of the material models is defined independently. This is performed using the erosion material model (`*MAT_ADD_EROSION`) to allow for failure and erosion of the elements and is commonly used to delete the elements [1, 2, 9, 33, 62, 63]. Default values are used except for the maximum effective strain at failure (`EFFEPS`) input. The values for this parameter are obtained from Prakash et al. [2] for each of the materials and are summarized in Table 2.7. Details of the element formulation and contact definitions used in the simulations are provided in Appendix A.3.

Continuum elements are used in the present model to enable coupling and interaction between interlaminar and intralaminar damage [42]. Specifically, damage initiation in the cohesive elements (i.e., interlaminar damage) begins from damage of the front ceramic layer (i.e., intralaminar damage) after impact. As the projectile penetrates, further fragmentation in the ceramic tile occurs, and the metal backing starts to deform which causes the delamination of layers. The interaction of the dif-

Table 2.4: Johnson-Holmquist II parameters used to define the alumina ceramic tiles in LS-DYNA [60].

Model Parameters	Value	Units
Density ( $\rho_{\text{JH2}}$ )	3700	kg/m <sup>3</sup>
Shear modulus ( $G_{\text{JH2}}$ )	$90.16 \times 10^9$	Pa
Intact strength constant ( $a_{\text{JH2}}$ )	0.93	-
Fractured strength constant ( $b_{\text{JH2}}$ )	0.31	-
Strain rate constant ( $c_{\text{JH2}}$ )	0	1/s
Fractured strength exponent ( $m_{\text{JH2}}$ )	0.6	-
Intact strength component ( $n_{\text{JH2}}$ )	0.6	-
Reference strain rate ( $\dot{\epsilon}_{\text{JH2},0}$ )	1	1/s
Maximum tensile strength ( $p^*$ )	$0.2 \times 10^9$	Pa
Maximum fracture strength ratio ( $SF_{\text{MAX}}$ )	0	-
Hugoniot elastic limit ( $HEL$ )	$2.79 \times 10^9$	Pa
Pressure at HEL ( $p_{HEL}$ )	$1.46 \times 10^9$	Pa
Bulking constant ( $\beta$ )	1	-
Damage constant ( $d_1$ )	0.005	-
Damage exponent ( $d_2$ )	1	-
Bulk modulus ( $k_1$ )	$130.95 \times 10^9$	Pa
Second pressure coefficient ( $k_2$ )	0	Pa
Third pressure coefficient ( $k_3$ )	0	Pa
Failure strain ( $FS$ )	1	-

Table 2.5: Johnson-Cook parameters used to define the aluminum Al5083 H116 metal backing and steel 4340 projectile in LS-DYNA [1, 61].

Model Parameters	Value (Aluminum)	Value (Steel)	Units
Density ( $\rho_{JC}$ )	2700	7860	kg/m <sup>3</sup>
Shear modulus ( $G_{JC}$ )	$26.9 \times 10^9$	$81.8 \times 10^9$	Pa
Yield stress ( $a_{JC}$ )	$0.520 \times 10^9$ [61]	$0.792 \times 10^9$	Pa
Hardening constant ( $b_{JC}$ )	$0.596 \times 10^9$	$0.510 \times 10^9$	Pa
Hardening exponent ( $n_{JC}$ )	0.551	0.26	-
Strain rate constant ( $c_{JC}$ )	0.001	0.014	-
Thermal softening exponent ( $m_{JC}$ )	0.859	1.03	-
Melting temperature ( $T_{melt}$ )	893	1790	K
Room temperature ( $T_{room}$ )	300	300	K
Reference strain rate ( $\dot{\epsilon}_{JC,0}$ )	1	1	1/s
Specific heat ( $C_P$ )	910	477	J/(kg.K)
Failure parameter 1 ( $D_1$ )	0.0261	0.05	-
Failure parameter 2 ( $D_2$ )	0.263	3.44	-
Failure parameter 3 ( $D_3$ )	-0.349	-2.12	-
Failure parameter 4 ( $D_4$ )	0.247	0.002	-
Failure parameter 5 ( $D_5$ )	16.8	0.61	-
Bulk modulus for the linear EOS ( $C_1$ )	$58.3 \times 10^9$	$159 \times 10^9$	Pa

Table 2.6: Mie-Gruneisen model equation of state parameters used to define the epoxy interlayer in LS-DYNA [1].

Model Parameters	Value	Units
Density ( $\rho$ )	1186	kg/m <sup>3</sup>
Intercept of the $v_s(v_p)$ curve ( $C$ )	2730	m/s
Unitless coefficient 1 slope of $v_s(v_p)$ curve ( $S_{MG,1}$ )	1.493	-
Gruneisen gamma ( $\gamma_0$ )	1.13	-

Table 2.7: Maximum effective strain at failure values for the erosion material model in LS-DYNA [1, 2]

Material	Maximum effective strain at failure
Alumina [1, 2]	2.0
Aluminum [1, 2]	2.0
Steel [1, 2]	2.1
Epoxy [1, 2]	1.5

ferent damage states in composite structures under impact has been reported in the literature [4]. Specifically, Shen et al. [4] reported the adhesive bonding performance (i.e., failure displacement) decreases with increasing adhesive thickness, thus having a negative effect on the overall ballistic performance of the ceramic layer. López-Puente et al. [32] also reported that there was an optimum adhesive layer thickness to get the best performance of the armor system.

Finally, a common element size range used for impact problems of a similar length scale is 0.1 mm to 1 mm [1, 33, 42, 43, 64–66]. In the current simulations, a coarse, medium, and fine mesh are generated using element sizes of 1 mm, 0.7 mm, and 0.5 mm, respectively. These meshes are generated using the finite element pre-processor, HyperMesh [57].

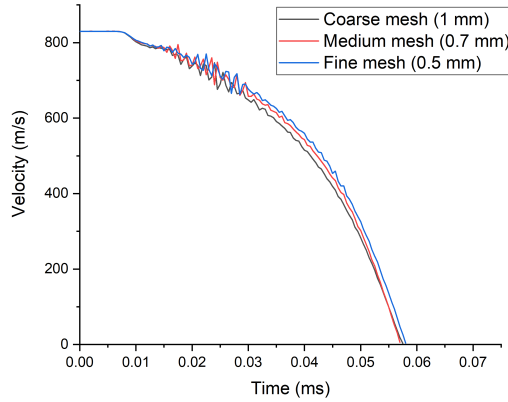


Figure 2.5: Results from the mesh sensitivity analysis using the velocity-time history of the rear center node of the projectile for the coarse (1 mm), medium (0.7 mm), and fine (0.5 mm) mesh sizes.

### Validating the ceramic/metal armor model

In this sub-section, the ceramic/metal armor model mesh will be validated with numerical results from Prakash et al. [2] and Rashed et al. [1]. The validation cases include a comparison of the velocity-time plot of the projectile and the DOP results. These criteria are chosen since they reasonably evaluate the performance of the armor system [1, 67].

At first, a mesh sensitivity analysis of the ceramic/metal armor model is conducted. Fig. 2.5 shows the velocity-time history plot of the rear center node of the projectile as it penetrates the layered structure. The rear node is selected for the time history as this was also done in the studies by both Prakash et al. [2] and Rashed et al. [1]. The results obtained are independent of the element size. Therefore, the medium mesh (0.7 mm) is selected for comparison. Fig. 2.6 shows that the velocity-time history plot of the rear center node of the projectile agrees well with the results provided by Prakash et al. [2] and Rashed et al. [1]. The next step is to validate the DOP results.

The second validation case compares the DOP results obtained with the coarse (1 mm), medium (0.7 mm), and fine (0.5 mm) mesh sizes. The DOP values for each mesh size are obtained by averaging over 6 nodes taken around the central axis at

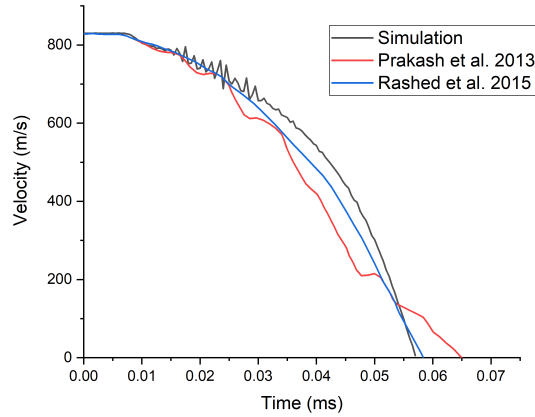


Figure 2.6: Velocity-time history of the rear center node of the projectile as it penetrates through the armor structure (using the medium mesh). Comparison is made with simulation results by Prakash et al. [2] and Rashed et al. [1].

Table 2.8: Depth of penetration results using coarse, medium, and fine element sizes. The absolute error difference is calculated relative to the results by Prakash et al. [2].

Mesh	Depth of penetration (mm)	Absolute error difference (%)
Coarse (1 mm)	12.8	8.6
Medium (0.7 mm)	13.9	0.8
Fine (0.5 mm)	14.1	0.6

the deepest location of the hole left by the impactor. The DOP results are presented in Table 2.8. An absolute percentage error difference is calculated in relation to the simulation results of Prakash et al. [2]. Altogether, Fig. 2.5 and 2.6, and Table 2.8 demonstrate that the three-dimensional impact model is implemented and validated reasonably with published data from the literature. In the next section, the epoxy adhesive that is initially used in the armor model is replaced by the SikaForce<sup>TM6</sup> 7752-L60 polyurethane adhesive model. The medium mesh size will be used in subsequent simulations.

## 2.4 Results and discussion

This section explores the effect of: (1) adhesive thicknesses, (2) defects in the adhesive layer, and (3) strain rate dependency in the model on the overall simulated ceramic/metal armor performance. Specifically, the armor performance is evaluated using a comparison of the velocity-history plot, depth of penetration (DOP) of the projectile, and damage patterns of the ceramic plate.

### 2.4.1 Effect of adhesive thickness

In this sub-section, the effects of different adhesive thicknesses are explored. Thicknesses varied from 0.50 mm to 1.50 mm with increments of 0.25 mm and are selected based on common thicknesses used in armor applications [2, 4, 9, 10, 32, 33]. To perform these simulations, the dependency of modes 1 and 2 critical energy release rates on the adhesive thicknesses is considered before their implementation in the model following [34]. Using Equation A.1 for mode I loading and Equation A.2 for mode II loading, the new critical energy release rates are evaluated based on the adhesive thickness. The values for  $\gamma_I$  and  $\gamma_{II}$  are first evaluated assuming values for  $\tau_I = 2690 \pm 700$  1/m and  $\tau_{II} = 1260 \pm 270$  1/m and these are taken from Marzi et al. [34] for the SikaForce<sup>TM6</sup> 498 epoxy adhesive. Using Equations A.1 and A.2 for the 1 mm adhesive thickness case, the  $\gamma_I = 2530 \pm 400$  N/m and  $\gamma_{II} = 38030 \pm 2840$  N/m values for the SikaForce<sup>TM6</sup> 7752-L60 polyurethane adhesive are then calculated. The  $G_{IC}$  and  $G_{IIC}$  values for all thicknesses are then calculated using Equations A.1 and A.2, and the results for these critical energy release rates are summarized in Table 2.9. The updated thickness-dependent values for  $G_{IC}$  and  $G_{IIC}$  are implemented in the CZM for the different adhesive thicknesses.

The velocity-time history curves of the rear center node of the projectile for the various adhesive layer thicknesses are presented in Fig. 2.7. The rear center node of the projectile is chosen to collect the velocity-time history curves to align with

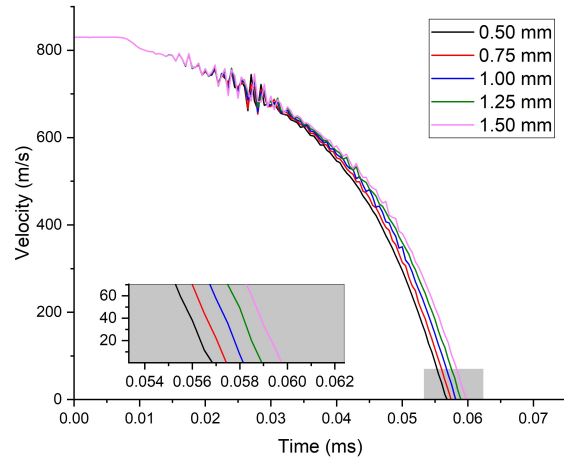
Table 2.9: Mode I and II critical energy release rates calculated for interlayer thicknesses of 0.50 mm to 1.50 mm.

Interlayer thickness (mm)	0.50	0.75	1.00	1.25	1.50
$G_{IC}$ (N/m)	1872	2195	2360	2444	2487
$G_{IIC}$ (N/m)	3530	4617	5410	5989	6411

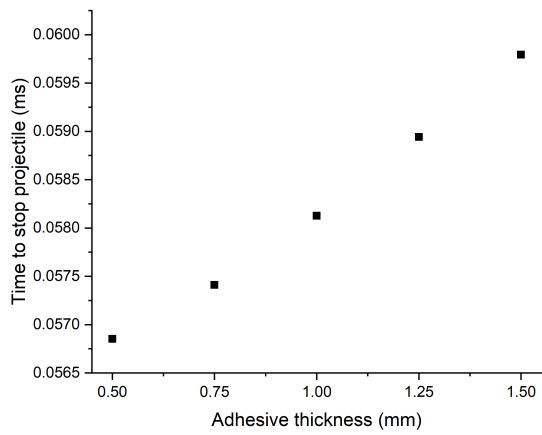
the other studies [1, 2]. Fig. 2.7 shows that the projectile takes longer to reach a complete stop with increasing adhesive thickness, suggesting a relatively inferior armor performance for single impact. While seemingly small, the differences of a few microseconds have been shown to be sufficient for influencing the ability of armor to defeat projectiles [68], including through erosion [67].

Next, the depth of penetration (DOP) is plotted against time for the different adhesive thicknesses in Fig. 2.8a. As before, the nodes at the deepest location of the hole left by the impactor are used to calculate the DOP for each thickness. The deviations of the DOP curves from using the various adhesive thicknesses begin to become more prominent at approximately 0.02 ms. This is the time it takes for the projectile to fully penetrate the ceramic layer and to start to penetrate the adhesive layer and metal backing. The DOP into the metal backing layer at the end of the simulation is plotted against adhesive thickness as shown in Fig. 2.8b. Here, the DOP increases with increasing adhesive layer thickness and this further suggests that for a single hit, an increase in adhesive thicknesses results in a decrease in armor performance under these conditions. The increasing DOP trend with increasing adhesive thickness is consistent with the study by Shen et al. [4].

Next, the resulting simulated damage patterns of the ceramic tiles for different adhesive thicknesses are presented in Fig. 2.9 where both the isometric and the cross-sectional views of the ceramic layers are shown. The damage pattern is not symmetric since an asymmetric projectile mesh is used for the simulation, with non-symmetric

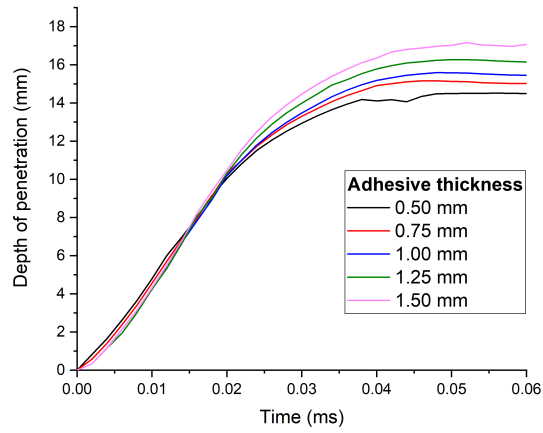


(a)

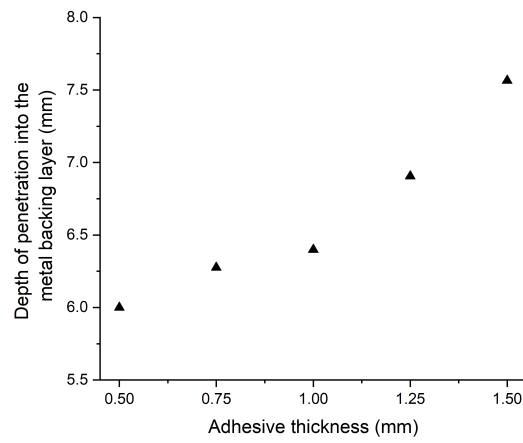


(b)

Figure 2.7: (a) Velocity-time history of the rear center node of the projectile and (b) time to stop projectile for adhesive layer thicknesses between 0.50 mm and 1.50 mm.



(a)



(b)

Figure 2.8: Depth of projectile penetration (a) plotted against time and (b) into the metal backing layer for adhesive thicknesses between 0.50 mm and 1.50 mm.

meshes being used elsewhere in the literature [69–72]. The overall damage area to the tiles decreases with increasing adhesive thickness. These damage areas weaken the top ceramic tile, thus a decrease in the multi-hit capability of the entire armor system would be expected if the damage was greater. In the literature, it has been shown that the structural integrity of the entire composite system can be weakened from small incremental damage states [43]. From this, the multi-hit capability is, therefore, expected to increase when increasing the adhesive thickness due to reduced fragmentation of the ceramic tiles around the point of impact. These trends with thickness and multi-hit capability are consistent with the ones presented by Shen et al. [4]. In summary, for the conditions simulated (single impact on ceramic/metal armor model), the best SikaForce<sup>TM6</sup> 7752-L60 polyurethane adhesive thickness was found to be 0.5 mm for the range of thicknesses investigated in this study. However, another optimization study must be performed to determine the best thickness for multi-impact conditions.

#### **2.4.2 The role of defects on simulated armor performance**

In this sub-section, the effect of introducing gaps or trapped air bubbles in the adhesive layer is explored using simulated voids within the layer. In real-world design, air bubbles can get trapped in the adherend due to the surface roughness during manufacturing, and can induce cracks leading to early or premature failure of an adhesive bond [73]. The gaps within the adhesive layer in these simulations represent structural defects that include inconsistencies in manufacturing and not material defects. In this current study, a MATLAB program is developed to randomly remove elements (specifically 0.5%, 1.5%, 2.5%, 3.75%, 5%, 6.25%, and 7.5% of air bubbles to total surface area ratios) from the interlayer, where these gaps are used to represent trapped air bubbles derived from manufacturing. In the code, element positions of the adhesive layer were extracted from the LS-DYNA keyword file, then random elements were deleted through a percentage input in the code. The new element po-

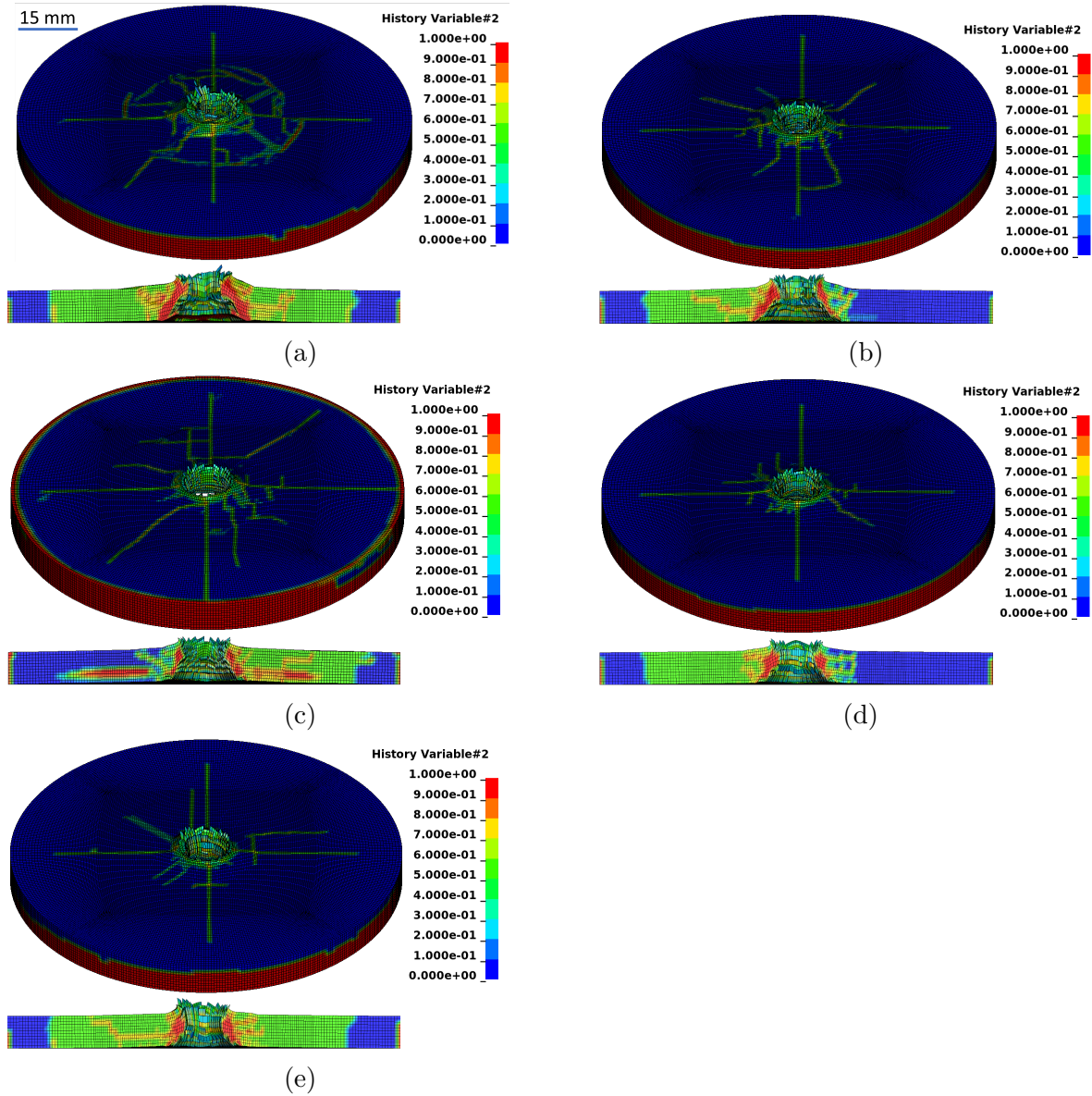


Figure 2.9: Damage patterns on the alumina ceramic tile for adhesive thicknesses of: (a) 0.50 mm, (b) 0.75 mm, (c) 1.00 mm, (d) 1.25 mm, and (e) 1.50 mm. A cross-sectional view of the ceramic tile is provided below the isometric view for each of the thicknesses.

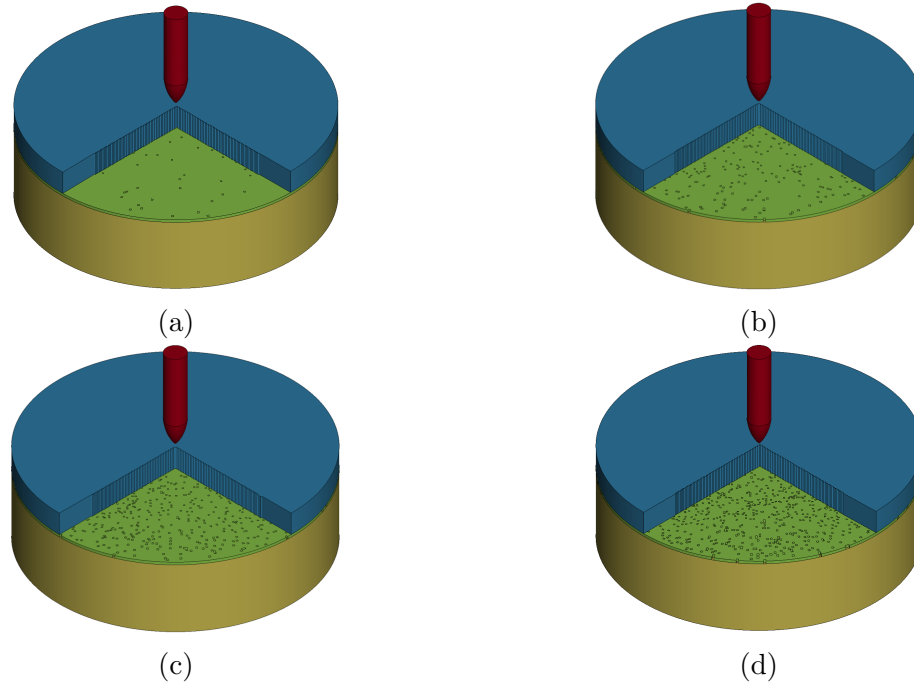


Figure 2.10: Air bubbles within the adhesive layer represented by deleted cohesive zone elements with gap ratios of: (a) 0.5%, (b) 2.5%, (c) 5%, and (d) 7.5%.

sitions were then imported back into the LS-DYNA keyword file. It is assumed that a quality control check is in place during manufacturing when bonding the ceramic to the metal backing and that the number of air bubbles to total surface area does not exceed 7.5%. A schematic showing these defects within the adhesive layer is provided in Fig. 2.10.

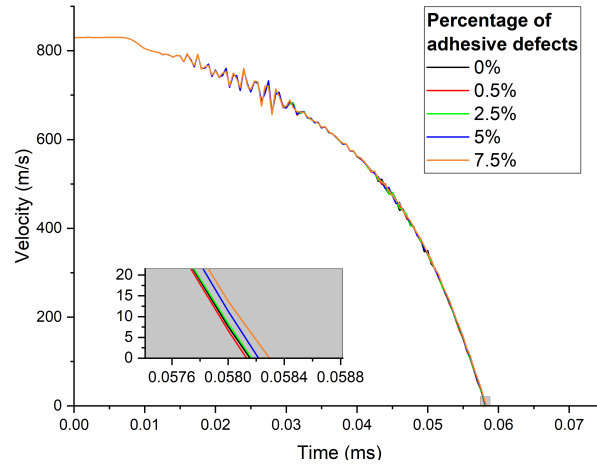
The effect of air bubbles on simulated armor performance is explored. For that purpose, the projectile velocity-time history for all the defect percentage ratios is presented in Fig. 2.11. This data represents five simulations at each porosity level. The low defect porosities (0% to 2.5%) results in similar times to stop the projectile, but the higher percentage of defects results in a greater time to stop the projectile ( $> 0.14$  microseconds). Again, it is very important to consider the small differences in microseconds for armor applications [67, 68]. The DOP of the projectile for the different defect percentage ratios is plotted in Fig. 2.12 where each point represents the average of five simulations taken as different realizations of random assignment

of defect locations. The error bars in Fig. 2.12 represent one standard deviation of the uncertainty under these considerations. As before, nodes at the deepest location of the impact crater are taken to calculate the depth of penetration under a given condition. From this figure, the percentage difference between the maximum and minimum DOP values is 0.9%. As seen in both Figs. 2.11 and 2.12, a small amount of defects can significantly affect armor performance. Results at low porosities of 0% to 2.5% defect percentage ratios in Fig. 2.12 suggest that there could be transitional behaviors of DOP for low defect porosities. The DOP and the time taken to stop the projectile at intermediate to high porosities of 2.5% to 7.5% defect percentage ratios are found to be higher than at low porosities. Therefore, the armor systems with the lower porosities within the adhesive layer result in lower DOP values, thereby potentially increasing the performance.

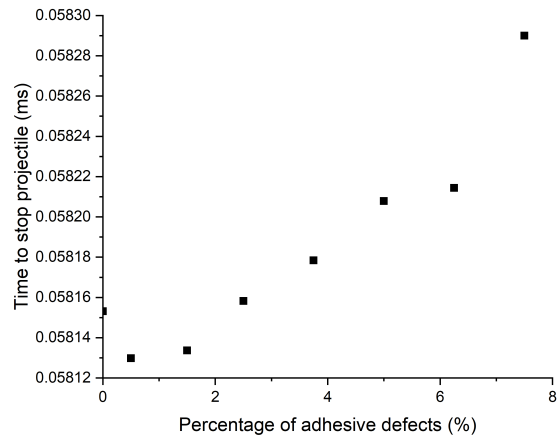
### 2.4.3 A strain rate-dependent cohesive zone model

Finally, the effects of introducing strain rate-dependent parameters on armor performance are explored. In the literature, similar rate-dependent trends have been reported for epoxy and polyurethane under high compressive loading rates [74] and so strain rate parameters for the 3M<sup>TM</sup> Scotch-Weld<sup>TM</sup> AF 163-2OST structural epoxy adhesive are implemented for the proposed SikaForce<sup>TM6</sup> 7752-L60 polyurethane adhesive cohesive zone model. The strain rate parameters for the epoxy adhesive are obtained from the study by Lißner et al. [75]. The parameters used for the strain rate-dependent cohesive zone model are summarized in Table 2.10.

To explore the effect of including strain rate dependency in the model on the response of the armor system, a comparison between the velocity-time responses measured at the rear center node for both cases (with and without strain rate dependency) is performed for three projectile velocities (630 m/s, 830 m/s, and 1030 m/s) and is shown in Fig. 2.13. In the velocity range studied, the results show that strain rate effects do not significantly affect the velocity-time profile, only a maximum of 0.8%



(a)



(b)

Figure 2.11: (a) Velocity-time history of the rear center node of the projectile (1.5%, 3.75%, and 6.25% porosities omitted for clarity) and (b) time to stop projectile for interlayer defect percentage ratios of 0% to 7.5%.

Table 2.10: Trilinear cohesive zone model parameters used to define the SikaForce<sup>TM6</sup> 7752-L60 polyurethane adhesive in LS-DYNA [26, 50, 51]. Strain rate dependency is considered by including rate-dependent terms of 3M<sup>TM</sup> Scotch-Weld<sup>TM</sup> AF 163-2OST structural epoxy adhesive [75].

Model Parameters	Value	Units
Density ( $\rho$ ) [50]	$1.60 \times 10^3$	kg/m <sup>3</sup>
Young's modulus ( $E$ ) [26]	$4.93 \times 10^8$	Pa
Shear modulus ( $G$ ) [26]	$1.88 \times 10^8$	Pa
Lower bound of yield strength ( $T_0$ ) [75]	$-3.24 \times 10^6$	Pa
Upper bound of yield strength ( $T_1$ ) [75]	$-1.80 \times 10^6$	Pa
Equivalent strain rate term of yield stress ( $\dot{\epsilon}_T$ ) [75]	0.1	-
Lower bound of shear strength ( $S_0$ ) [75]	$-5.16 \times 10^6$	Pa
Upper bound of shear strength ( $S_1$ ) [75]	$-1.60 \times 10^6$	Pa
Equivalent strain rate term of shear stress ( $\dot{\epsilon}_S$ ) [75]	0.1	-
Lower bound of mode I critical energy release rate ( $G_{I0}$ ) [75]	$-2.36 \times 10^3$	N/m
Upper bound of mode I critical energy release rate ( $G_{I\infty}$ ) [75]	$2.00 \times 10^3$	N/m
Equivalent strain rate term of mode I critical energy release rate ( $\dot{\epsilon}_{GI}$ ) [75]	0.1	-
Lower bound of mode II critical energy release rate ( $G_{II0}$ ) [75]	$-5.41 \times 10^3$	N/m
Upper bound of mode II critical energy release rate ( $G_{II\infty}$ ) [75]	$6.5 \times 10^3$	N/m
Equivalent strain rate term of mode II critical energy release rate ( $\dot{\epsilon}_{GII}$ ) [75]	0.1	-
Mode I plastic to total area ratio ( $f_{G1}$ ) [51]	0.13	-
Mode II plastic to total area ratio ( $f_{G2}$ ) [51]	0.9	-

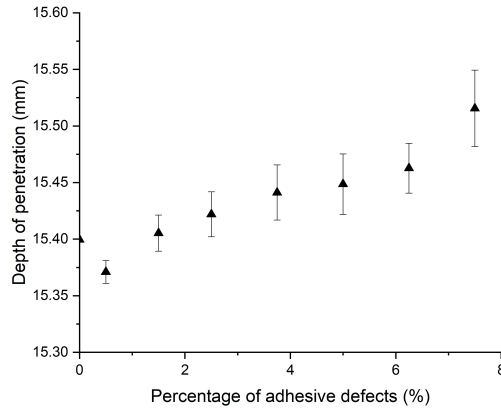


Figure 2.12: Depth of projectile penetration for interlayer defect percentage ratios of 0% to 7.5%.

difference between the two curves for the 830 m/s case. The strain rate effects do not affect the results significantly since the stopping power of the adhesive is minimal. The mechanical response of the adhesive is, however, important for damage induced by high velocity impact since it is related to the bonding and failure of elements. Next, the DOP results obtained for these projectile velocities for both the model with and without strain rate-dependent terms are presented in Table 2.12. As expected, the DOP increases when increasing the impact velocity for both cases. When including strain rate dependency, there is a negligible DOP increase where at the highest velocity the difference is 0.87 mm.

One significant difference between the two models is the damage area of the adhesive under the impact zone. Schematics of these damage zones for both the model with and without strain rate-dependent terms are presented in Fig. 2.14 for the 830 m/s case. Similar trends are seen with the other initial velocities, so only the 830 m/s case is presented here. The area of the damage zone (or deleted elements) for the different velocity cases with and without considering strain rate is calculated and presented in Table 2.11. The 830 m/s case results in the greatest damage area for both the strain rate and non-strain rate-dependent adhesive models. More importantly, the inclusion of strain rate-dependent terms in the model results in a much

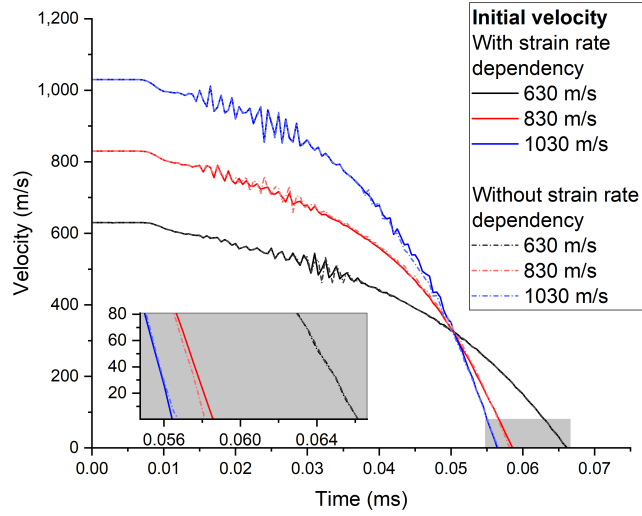


Figure 2.13: Velocity-time history of the rear center node of the projectile for initial projectile velocities of 630 m/s, 830 m/s, and 1030 m/s with and without the strain rate-dependent model implemented for the adhesive layer constitutive model.

larger debonding area for all velocities. This suggests that a decrease in the multi-hit capability of the multilayered structure would be predicted if strain rate dependency was considered due to the larger debonding area of the ceramic layer from the metal backing layer.

Table 2.11: Adhesive damage area after impact for initial projectile velocities of 630 m/s, 830 m/s, and 1030 m/s with and without the strain rate terms implemented in the adhesive layer constitutive model.

Initial velocity (m/s)	Damage area (mm <sup>2</sup> )	
	With strain rate terms	Without strain rate terms
630	870	252
830	2047	421
1030	1690	386

Table 2.12: Depth of penetration results for initial projectile velocities of 630 m/s, 830 m/s, and 1030 m/s with and without the strain rate terms implemented in the adhesive layer constitutive model.

Initial velocity (m/s)	Depth of penetration (mm)	
	With strain rate terms	Without strain rate terms
630	13.39	13.45
830	14.05	15.57
1030	19.81	20.68

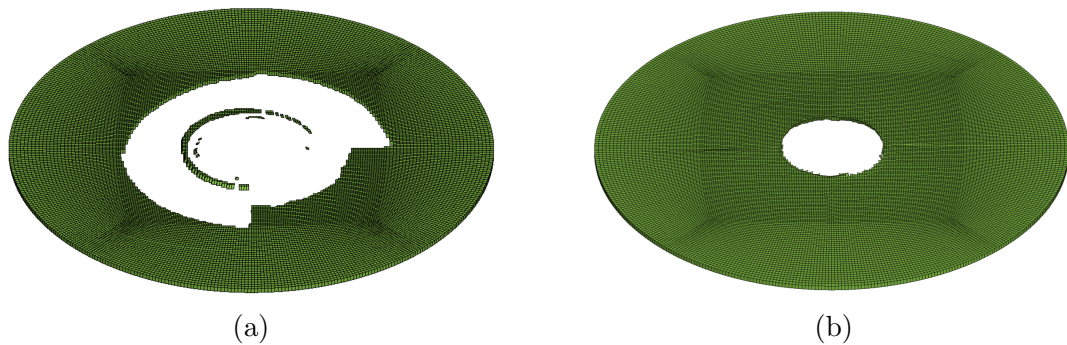


Figure 2.14: The damage region of the adhesive (a) with and (b) without implementing the strain rate-dependent terms into the cohesive zone model for the projectile travelling at an initial velocity of 830 m/s.

## 2.5 Conclusions

For the first time in the literature, a trilinear cohesive zone model is developed and validated for the SikaForce<sup>TM6</sup> 7752-L60 polyurethane adhesive to model all phases of its dynamic failure, including elasticity, plasticity, and damage initiation. The model is validated using force-displacement curves of double cantilever beam and end-notched flexure tests published by Faneco et al. [26]. A system-scale armor model consisting of a ceramic tile bonded to an aluminum backing is validated using numerical data such as the velocity-time history and depth of penetration of the projectile. The validated cohesive zone adhesive model for the SikaForce<sup>TM6</sup> 7752-L60 polyurethane is then implemented into the validated system-scale armor model. This work presents new approaches to analyze and explore the armor model by: (1) investigating the effects of

using different interlayer thicknesses and considering the dependency of critical energy release rates to material thickness, (2) introducing adhesive layer defects (manufacturing defects resulting from trapped air bubbles) through a developed MATLAB script to delete random cohesive elements, and (3) incorporating strain rate terms into the adhesive cohesive zone model. Thicker adhesive layers are found to increase the time taken for the projectile to stop and also increase the depth of penetration, thus decreasing simulated armor performance. An increase in the adhesive thickness, however, reduces the damage to the ceramic tile of the layered structure through a subsequent reduction in the damage area of the impact zone. An increase in the percentage of air bubbles in the adhesive layer led to an increasing trend in the depth of penetration and longer times to stop the bullet. Thus, this increase in air bubbles within the adhesive layer would lead to lower ballistic performance in these systems. Introducing the strain rate-dependent terms in the model led to a significant increase of the adhesive debonding/damage region under the impact zone and a decrease in the depth of penetration for all the projectile velocities. Overall, this study opens to: (1) improve upon existing adhesive models to better describe their dynamic behavior under high-velocity impact loadings, and (2) guide the design of armor systems to improve their performance.

# Chapter 3

## Design of micro- and macro-scale polymeric metamaterial solutions for passive and active thermal camouflaging applications

Submitted as **Harshil Pisavadia**; A. Asad; D. Sameoto; P. Dolez; and J.D. Hogan.  
*Design of Micro- and Macro-scale Polymeric Metamaterial Solutions for Passive and Active Thermal Camouflaging Applications*. Advanced Physics Research. (2022)

---

Author	Contributions
Harshil Pisavadia	Conceptualization, Methodology, Software, Validation, Formal analysis, Writing - Original Draft, Visualization
Asad Asad	Writing - Review & Editing
Dan Sameoto	Conceptualization, Writing - Review & Editing
Patricia Dolez	Writing - Review & Editing, Supervision
James Hogan	Principal investigator, Conceptualization, Writing - Review & Editing, Supervision

---

## 3.1 Abstract

This work utilizes predictive modelling techniques to guide and inform metamaterial design for heat management solutions and thermal radiation control. Specifically, micro- and macro-scale polyethylene-based solutions are proposed for passive and active thermal camouflage. A micro-scale post design is proposed for highly-tunable infrared emissivity based on varying unit cell geometrical configurations. Actively modulating these micro-features through lateral straining of up to 3% allows for red-shifting the emissivity spectrum by up to 0.5  $\mu\text{m}$ . Macro-scale lenticular lens designs allow for a more passive form of camouflage due to its emissive stability for a range of configurations (e.g., single and sandwiched structures, increasing lens radii and height). Overall, the proposed metamaterial designs allow the tailoring of optical properties to improve thermal radiating performance.

## 3.2 Introduction

Tunable mid-infrared (MIR) emitting surfaces and improved infrared (IR) camouflage solutions is an area of high interest by militaries around the world due to hyperspectral imaging technologies being more available. Tunable MIR emissivity in adaptive artificial optical materials is an important metric for various applications including heat management or radiative cooling [76, 77], thermal emitters [78], thermophotovoltaic cells [79], infrared communication [80], and thermal camouflage [81, 82]. Metamaterials allow for flexibility in tuning the surface emissivity, which can be achieved by various modulation methods including phase changes [16, 83], altering crystal orientation angles [81], and electric modulation [84]. However, the majority of this work is conducted experimentally [85–88]. To date, limited studies have applied predictive modelling techniques to inform design decisions for IR management surfaces [21, 24, 89]. This article develops predictive modeling capabilities to inform metamaterial structural designs for active and passive thermal signature management solutions.

The two main approaches to achieve and realize IR camouflage are to (1) decrease the surface temperature by reducing thermal radiation through insulation [90–92] and (2) control and tune the surface emissivity spectrum [12, 81, 83, 93]. Metamaterials have been extensively used for thermal camouflaging applications as they can manipulate the optical properties of materials (e.g., reflectivity, transmittivity, and emissivity) through varying their geometrical and optical material parameters [12, 22, 24, 81]. For example, Lee et al. [13] developed a metal-dielectric-metal metamaterial to tune the emissivity towards favorable bands (i.e., wavelengths within the non-atmospheric window of 5 to 8  $\mu\text{m}$ ) for radiative cooling applications for aircraft which would otherwise be easily viewed in the atmosphere. In another study, Dang and Ye [24] proposed utilizing photonic crystalline structures to realize (1) heat dissipation by increasing the emittance in the hidden bands within the non-atmospheric window, and (2) thermal camouflage by decreasing emissivity within the atmospheric window (wavelengths from 3 to 5  $\mu\text{m}$  and 8 to 14  $\mu\text{m}$ ).

In the literature, the majority of geometrical scales for metamaterial-based IR camouflaging technologies are within the micro-scale regime ( $< 50 \mu\text{m}$ ) to promote Mie scattering [12, 82, 94]. For example, micro-features in the form of cylindrical disk configurations are predominantly used as IR emissive tunable surfaces [16, 83, 89]. One challenge regarding these micro-scale structures is their manufacturing [82] which requires a multi-step fabrication process that may cause premature deterioration [95]. Increasing the geometric length-scale to the macro-scale ( $> 100 \mu\text{m}$ ) could reduce the complexity and enhance the scalability of these manufacturing processes. To date, no studies have utilized lenticular lenses (experimentally or numerically) to promote optical scattering over Mie scattering for IR camouflage.

Building on past works, the focus of this study is to develop predictive models using COMSOL Multiphysics<sup>®</sup> [96] to inform design decisions when manufacturing polyethylene (PE)-based micro- and macro-scale metamaterials for passive and active thermal camouflaging applications within the MIR wavelength (5 to 16  $\mu\text{m}$ ). PE is

the polymer of choice for this study due to its low emissive properties [95, 97, 98], ability to be woven into fibers for smart textile applications [99], elastic durability [100], and high IR transparency [28]. For the first time in the literature: (1) PE-based patterned metamaterials (specifically, micro- and macro-scale designs) for passive and active thermal management solutions are proposed, (2) a lenticular lens macro-scale design in various configurations (e.g., single-layered and multi-layered systems) is explored for efficient thermal management, (3) active solutions to thermal radiation control are introduced where elastic properties of PE are used to dynamically change the geometrical aspect ratio of the unit cells of metamaterials, and (4) preferable configurations for micro-scale post design (post height, width, and spacing) are proposed. The results are discussed in the context of manufacturing metamaterials for thermal radiation control. Overall, we seek to tailor optical properties (e.g., emissivity and scattering) by designing micro- and macro-scale surface features in PE metamaterials towards our goal of informing more efficient thermal camouflage designs.

### 3.3 Results and discussion

In this study, the Electromagnetic Waves Frequency Domain interface within the radio frequency (RF) module in COMSOL Multiphysics<sup>®</sup> is used to simulate the interaction between IR light and three-dimensional (3D) micro- and macro- scale geometries. In particular, Fresnel equations are used to evaluate absorptivity, emissivity, reflectivity, and transmittivity through scattering parameters (S-parameters) [101].

Emissivity ( $E$ ) and absorbance ( $A$ ) properties of materials are dependent on their reflectivity ( $R$ ) and transmittivity ( $T$ ) through Kirchhoff's law of thermal radiation ( $E = A = 1 - R - T$ ) [102]. These reflectivity and transmittivity values are dependent on geometrical features and optical properties [13, 17, 94]. Furthermore, the thermal radiation ( $P$ ) of a material is dependent on its emissivity through the Stefan-Boltzmann law ( $P = E\sigma T^4$ ) where  $\sigma$  is the Stefan-Boltzmann constant and  $T$  (K) is the surface temperature. Therefore, the above relationship allows the optical

properties to be used as performance indicators of IR camouflage. Controlling the geometrical features of metamaterials can shift and tune emissivity values to improve their radiative thermoregulating performance.

This section starts by discussing the validation of the polyethylene material model. Next, three polyethylene-based metamaterial configurations are explored for passive and active thermal camouflaging applications: (1) macro-scale single-layered lenticular lens design, (2) macro-scale sandwiched lenticular lens design, and (3) micro-scale post design.

### 3.3.1 Polyethylene material model validation

This section discusses the validation of the PE material model, as shown in Figure 3.1. Experimental data of a plain unstructured 10  $\mu\text{m}$  PE sheet from Chen et al. [28] is used to validate the material model. Figure 3.1a shows a schematic of a unit cell geometry consisting of a plain 10  $\mu\text{m}$  thick PE sheet exposed to air. Here, the IR rays are orthogonal to the sheet via the input port. The input port also measures the reflected waves from the interaction. Transmittivity is calculated via the output port at the bottom of the PE sheet. In our simulations, the micro-sized features (e.g., lens, posts, sandwich structures) are modelled as unit cells with Floquet periodic boundary conditions in the x- and y- directions. In addition, perfectly matched layers (PMLs) are used above the homogeneous medium (air) along the propagation direction to absorb reflected and radiated waves while minimizing surface reflections. This setup is similar to others in the literature [24, 103, 104].

In this study, the PE material model is simulated using the loss tangent dissipation factor electric displacement field model. Shown in Figure 3.1b is the loss-tangent to wavelength input. Here, the loss tangent is not constant and is instead dependent on the wavelength and frequency of light [105] where peaks are observed in the infrared regime due to ionic mechanisms of the material [106]. In the case of PE-based polymers within the IR regime, these peaks result from the carbon-hydrogen (C-H) and

carbon-carbon (C-C) bonds. Our model informs the loss tangent values for the MIR spectrum which is in turn used to validate the emittance spectrum.

Comparisons between the experimentally obtained emissivity/absorptivity curves from Chen et al. [28] and simulated results for a plain 10  $\mu\text{m}$  thick PE sheet are presented in Figure 3.1c. Both the experimental and simulated curves are in close agreement, and therefore, the PE material model is considered validated. Additional work in the literature supports a similar validation procedure [11, 14]. Furthermore, a unit cell width sensitivity study was conducted (by varying cell widths from 10 to 50  $\mu\text{m}$ ), where the magnitudes and locations of peaks within the emissivity spectrum were not found to be sensitive to the specified length scales.

Finally, the sensitivity of transmittance to PE thicknesses (between 1-350  $\mu\text{m}$ ) is presented in Figure 3.1d in a semi-log plot. Each data point represents the area under the transmittivity curve to evaluate its transparency for each specific sheet thickness. As expected, thinner sheets have a greater overall transmittivity suggesting greater transparency than thicker sheets. Overall, the transmittivity decreases as the PE sheet thickness increases. Therefore, the validated material model can now be used for a wide range of PE sheet thicknesses (from 1 to 350  $\mu\text{m}$ ), thus being suitable for both micro- and macro-scale based design for thermal radiation control [17, 107].

### 3.3.2 Macro-scale single-layered lenticular lens design

This sub-section explores macro-scale single-layered lenticular lens designs for improving radiative thermoregulating performance, as shown in Figure 3.2. Figure 3.2a shows the global overall lens geometry where the inset image shows a unit cell of the lens structure. Here,  $P$  is the width of the unit cell,  $t_p$  is the base sheet thickness,  $r$  is the lens radius, and  $h$  is the lens height. Figure 3.2b shows the resulting emissivity/ absorptivity curve within the MIR spectrum for increasing radii from  $r = 100$  to 750  $\mu\text{m}$  and corresponding lens height from  $h = 78$  to 6  $\mu\text{m}$ . These configurations are selected from our experience in manufacturing these structures and their optical

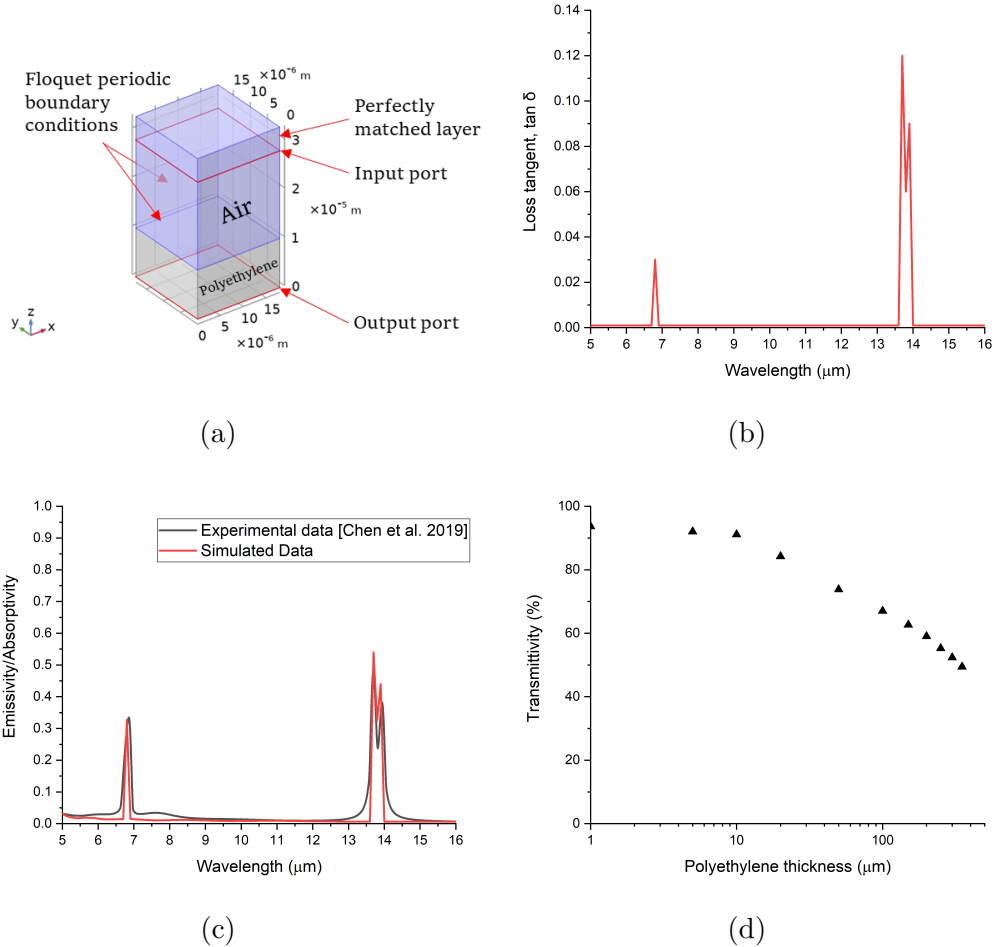


Figure 3.1: COMSOL Multiphysics<sup>®</sup> model validation of a plain unstructured polyethylene sheet. (a) Unit cell geometry of a plain 10  $\mu\text{m}$  thick polyethylene sheet with corresponding locations of boundary conditions. Additional Floquet periodic boundary conditions are used in the x- and y- directions. (b) Loss tangent-wavelength input plot to COMSOL Multiphysics<sup>®</sup> for a plain 10  $\mu\text{m}$  thick polyethylene sheet. (c) Validated emissivity output for a 10  $\mu\text{m}$  thick polyethylene film for the infrared spectrum (wavelengths of 5-16  $\mu\text{m}$ ). (d) Sensitivity of transmittivity results to polyethylene thickness, where the overall transmittivity decreases with increasing thickness in the infrared spectrum (wavelengths of 5-16  $\mu\text{m}$ ).

scattering properties, noting that none of these have been considered before in the literature. A gradual increase in the overall emissivity for increasing wavelengths is seen across all the radii. This suggests that these structures result in emissive stability across all configurations chosen here, which, again, is motivated by our ability to manufacture these structures. Shown in Figure 3.2c is the resulting optical properties (emissivity/absorptivity and reflectivity) for varying angle of incidence ( $\theta = 0^\circ$  to  $60^\circ$ ) where a shift in the optical properties is observed. This behavior suggests high dispersion and scatter of MIR waves from their interaction with the lens structures, which has been observed to be favorable for cloaking applications [108, 109]. Finally, the contour plot in Figure 3.2d shows the effect of applying a lateral strain ( $\varepsilon = 0$  to 0.03) to the lenticular unit cell on resulting shifts in wavelength (x-axis); the single lenticular unit cell with the direction of strain is depicted in the inset. Previous manufacturing studies have used strain actuation for IR emissivity tuning with favorable results [85, 86], and this motivates our computational exploration here. In Figure 3.2d, applying lateral strains of up to the linear strain limit of PE of  $\varepsilon = 0.03$  [100] does not have a significant effect on the emissivity of the structure (due to the geometrical scale being larger than the MIR wavelength range), further suggesting a stable emissive configuration is achieved with lenticular lens structures, and this is desirable for passive forms of thermal management.

### 3.3.3 Macro-scale sandwiched lenticular lens design

This sub-section explores the macro-scale lenticular lens design within a sandwiched configuration with orthogonally oriented lenses, as presented in Figure 3.3. Figure 3.3a shows the overall geometry of the sandwiched structure (lens facing inwards) considered here, where the inset image shows a unit cell of the configuration. Here,  $t_{air}$  is the air gap between the two base sheets of the lenses. A lens facing outwards configuration is also explored under the same orthogonally oriented lenses configuration. Shown in Figure 3.3b and 3.3c is the emissivity plotted against the MIR wavelength

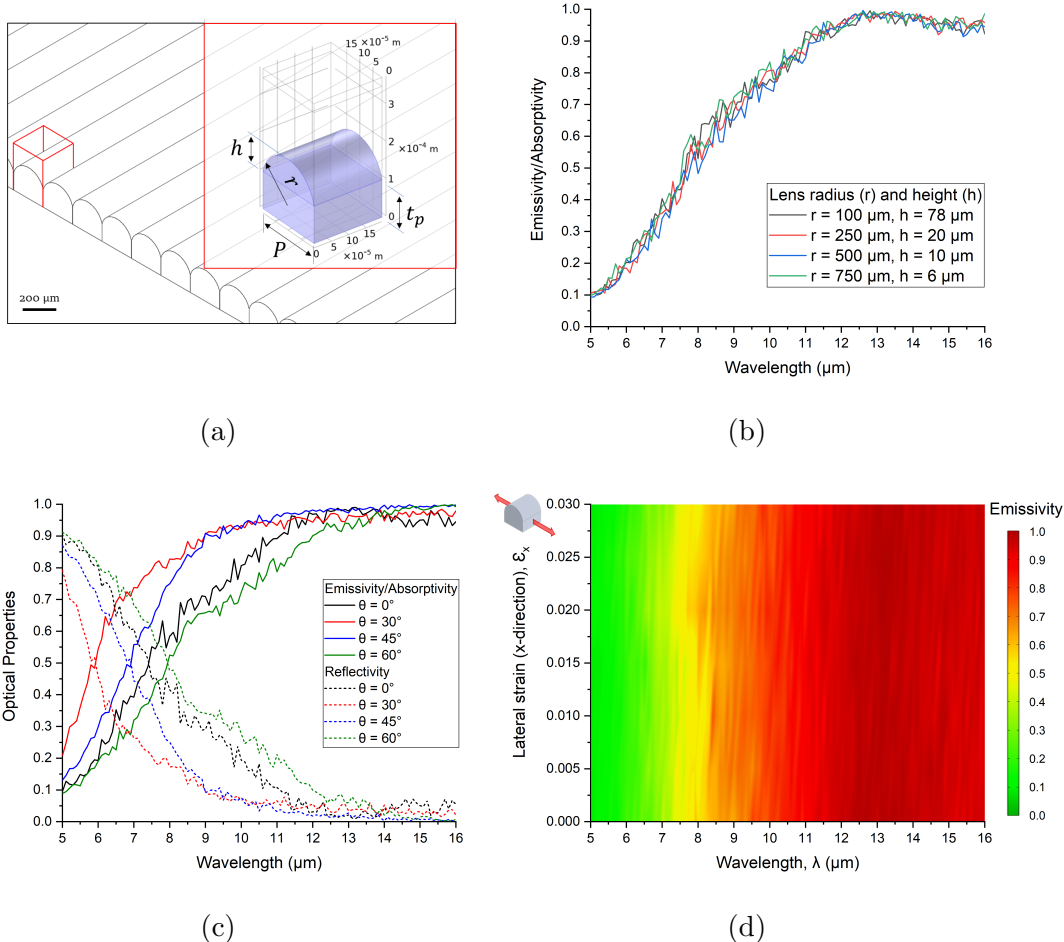
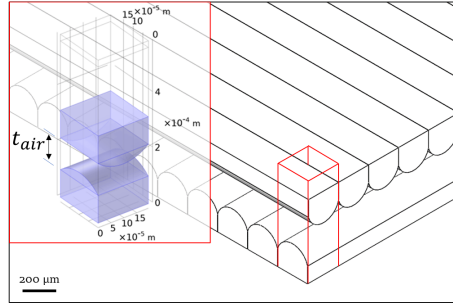


Figure 3.2: Simulating the macro-scale lenticular lens design in COMSOL Multiphysics<sup>®</sup>. (a) Global overall lenticular lens geometry. The inset image shows a unit cell geometry where  $P = 195 \mu\text{m}$ ,  $r = 100 \text{ to } 750 \mu\text{m}$ ,  $h = 78 \text{ to } 6 \mu\text{m}$ , and  $t_p = 100 \mu\text{m}$ . (b) Emissivity spectrum of the lenticular lens design with change of lens radius ( $r = 100 \text{ to } 750 \mu\text{m}$  and  $h = 78 \text{ to } 6 \mu\text{m}$ ). (c) Emissivity/absorptivity and reflectivity spectra of the lenticular lens design ( $r = 150 \mu\text{m}$  and  $h = 78 \mu\text{m}$ ) for varying angles of incidence ( $\theta = 0^\circ \text{ to } 60^\circ$ ) suggesting a high dispersion of rays. (d) Spectral emissivity of the lenticular lens design ( $r = 150 \mu\text{m}$  and  $h = 78 \mu\text{m}$ ) with an applied lateral strain in the x-direction ( $\epsilon_x = 0 \text{ to } 0.03$ ). The inset image shows representative radii of the unit cell with applied lateral strain in the x-direction (not to scale). The macro-scale lenticular lens design allows for a high dispersion of rays while being stable under varying lens radii and strains.

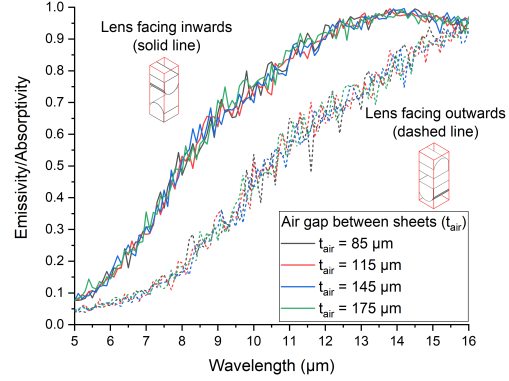
for increasing air gaps ( $t_{air} = 85$  to  $175 \mu\text{m}$ ) and lens radii ( $r = 100$  to  $750 \mu\text{m}$ ) for both the lens facing inwards and outwards configurations. Similar trends to the single lenticular lens design are observed where the emissivity gradually increases for increasing wavelengths for all radii and air gaps. The lens facing inwards configuration, however, exhibits greater emissivity throughout the entire MIR spectrum for all air gaps and lens radii. Other studies, however, found smoother surfaces exhibit lower emissivity values than with rough surfaces [110, 111]. Furthermore, emissive stability within each of the configurations for all radii and air gaps is seen. Finally, Figure 3.3d shows the resulting optical properties (emissivity/absorptivity and reflectivity) for varying angle of incidence ( $\theta = 0^\circ$  to  $60^\circ$ ) for the lens facing outwards configuration. The shift in optical properties from varying the angle of incidence suggests high optical scattering resulting from the interaction.

### 3.3.4 Micro-scale post design

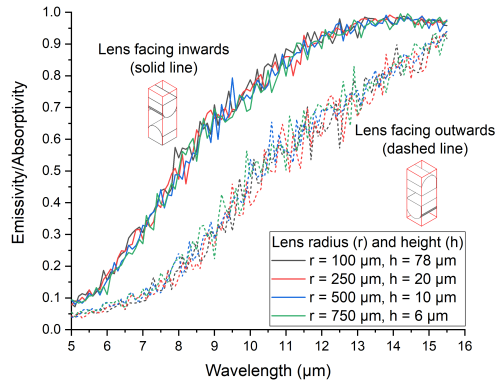
In this final sub-section, a micro-scale post design is simulated as shown in Figure 3.4. The overall geometry is presented in Figure 3.4a with the unit cell configuration shown in the inset image. Here,  $a$  is the post width,  $h$  is the post height,  $b$  is the post spacing, and  $t_p$  is the base sheet thickness. Figure 3.4b shows the emissivity spectrum for various configurations of the post design ( $a = h = 1, 5,$  and  $9 \mu\text{m}$ , and  $b = 1, 5,$  and  $9 \mu\text{m}$ ), motivated by similar sized disk configurations in the literature [17, 24]. Within these configurations, three bands exist which are governed by the post width and height. The smallest post width ( $a = 1 \mu\text{m}$ ) has a similar emissivity spectrum to a plain PE sheet (Figure 3.1c) where peaks exist due to the ionic mechanisms in the material [106]. This response is comparable to what our team has observed experimentally and is attributed to the geometrical scale of the micro-features and spacings being outside of the MIR wavelength range. Other studies found increasing disk sizes result in a blueshift of emissivity [13, 89], whereas in our study, increasing the post width increases overall emissivity in a non-linear manner. Furthermore,



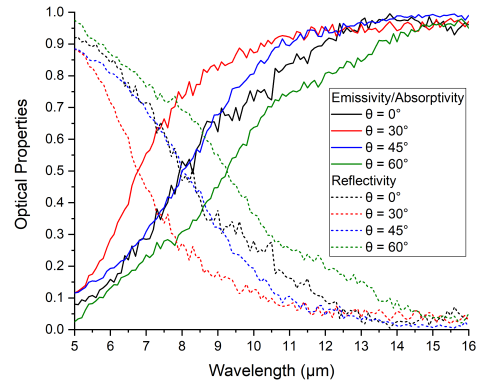
(a)



(b)



(c)



(d)

Figure 3.3: Simulating the macro-scale lenticular lens sandwiched structure design in COMSOL Multiphysics<sup>®</sup>. (a) Global overall sandwiched lenticular lens geometry (lens facing inwards) with air between the sheets. The inset image shows a unit cell geometry where  $t_{air} = 85$  to  $175 \mu\text{m}$ ,  $r = 100$  to  $750 \mu\text{m}$ ,  $h = 78$  to  $6 \mu\text{m}$ , and  $t_p = 100 \mu\text{m}$ . The configuration with the lens facing outwards is also investigated. Emissivity spectrum of the lenticular lens sandwiched structure with change of: (b) air gap between the lenticular lens sheets ( $t_{air} = 85$  to  $175 \mu\text{m}$ ); and (c) change of lens radius ( $r = 100$  to  $750 \mu\text{m}$  and  $h = 78$  to  $6 \mu\text{m}$ ) for both lens facing inwards and outwards configurations. The lens facing outwards design has a lower emissivity within the mid-infrared wavelengths for all lens radii and air gaps. (d) Emissivity/absorptivity and reflectivity spectra of the lenticular lens sandwiched structure (lens facing inwards,  $r = 150 \mu\text{m}$  and  $h = 78 \mu\text{m}$ ) for varying angles of incidence ( $\theta = 0^\circ$  to  $60^\circ$ ). Similar trends are observed for the lens facing outwards configuration. A high dispersion of rays is evident from the shift of optical properties due to varying angles of incidence of the IR light, while demonstrating emissive stability under the various geometrical configurations.

emissivity peaks are generated with greater post spacings. The optical properties (emissivity/absorptivity and reflectivity) for varying angles of incidence ( $\theta = 0^\circ$  to  $60^\circ$ ) for the  $a = 9 \mu\text{m}$  and  $b = 5 \mu\text{m}$  configuration are plotted in Figure 3.4c, where this configuration is chosen because a high emissive response is observed within the hidden non-atmospheric band (i.e., wavelengths from 5 to 8  $\mu\text{m}$ ). The variation in peaks due to the incident angle suggests high dispersion and scatter of rays. Finally, the strain configurations for the unit cell of the posts for up to  $\varepsilon = 0.03$  are shown in Figure 3.4d for the  $a = 9 \mu\text{m}$  and  $b = 5 \mu\text{m}$  configuration where emissivity is found to redshift by values of up to 0.5  $\mu\text{m}$ . It should be noted that applying strains to the micro-scale post design redshift emissivity to a much greater degree than the macro-scale lenticular lens design, although the manifestation of these shifts for performance needs to be evaluated.

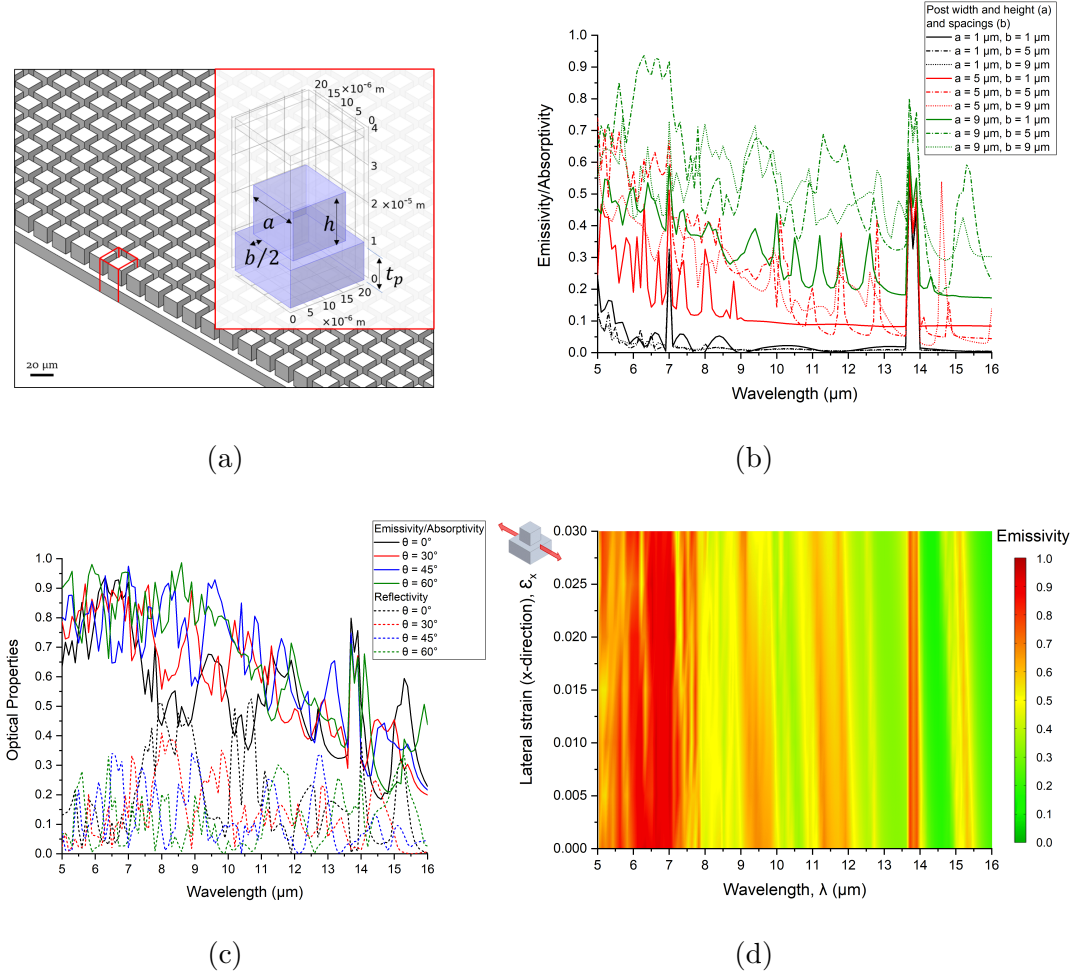


Figure 3.4: Simulating the micro-scale posts design in COMSOL Multiphysics<sup>®</sup>. (a) Global overall post geometry. The inset image shows a unit cell geometry where  $a = 1$  to  $9 \mu\text{m}$ ,  $b = 1$  to  $9 \mu\text{m}$ ,  $h = 1$  to  $9 \mu\text{m}$ , and  $t_p = 10 \mu\text{m}$ . (b) Emissivity spectrum of the post lens design with change in post size and spacing where  $a = 1$  to  $9 \mu\text{m}$ ,  $b = 1$  to  $9 \mu\text{m}$ , and  $h = 1$  to  $9 \mu\text{m}$ . (c) Emissivity/absorptivity and reflectivity spectra of the post configuration ( $a = 9 \mu\text{m}$  and  $b = 5 \mu\text{m}$ ) for varying angles of incidence ( $\theta = 0^\circ$  to  $60^\circ$ ). (d) Spectral emissivity of the post configuration ( $a = 9 \mu\text{m}$  and  $b = 5 \mu\text{m}$ ) with an applied lateral strain in the x-direction ( $\epsilon_x = 0$  to  $0.03$ ). Micro-sized posts allow for highly-customizable solutions for thermal radiation control.

### 3.4 Conclusion

In summary, predictive models were developed in this study for polyethylene-based 3D micro- and macro-scale metamaterial solutions for thermal radiation control. In this study, the three designs explored for IR camouflaging capabilities are: (1) macro-scale lenticular lens design, (2) macro-scale lenticular lens sandwiched structure, and (3) micro-scale post design. Both the single and sandwiched lenticular lens designs exhibited similar stable emissive trends with high optical light dispersion capabilities, which is efficient for passive camouflage. The micro-scale post design allows highly-customizable solutions to tune the emissivity response of the metamaterials. Actively actuating the post design through strain modulation techniques is a viable option to redshift the emissivity spectrum. Overall, this study (1) aims to guide design decisions for tunable IR emitting surfaces and thermal radiation control using predictive modelling capabilities and (2) demonstrates how practical changes in surface topology result in measurable changes in optical properties.

# Chapter 4

## Concluding remarks

### 4.1 Implications

This thesis explored multi-functional add-on hybrid armor models and designs used for vehicle protection including: (1) the development and integration of the adhesive interlayer for ceramic/metal armor applications of land vehicles using cohesive zone modelling techniques, and (2) developing and exercising optical models to guide design choices and geometries (e.g., shapes and sizes of micro-sized features) of polyethylene-based metamaterials used for thermal camouflage applications. The main contributions of this thesis are summarized below:

1. This thesis presents a novel approach to model the adhesive layer for ceramic/metal armor using the trilinear cohesive zone approach. This method considers the ductile properties of polyurethane adhesives, which are commonly used in these types of systems. Furthermore, strain rate effects are considered to accurately predict the complex failure modes of delamination upon impact. Strain rate effects have an important role in predicting the delamination zone of the layered armor structure.
2. Thickness has been considered as a critical parameter when simulating adhesives in these systems. Here, the critical energy release rate (in tensile and shear modes) is considered to be a function of adhesive thicknesses, which has not

yet been considered in the literature for impact simulations on ceramic/metal armor. These material property considerations are crucial for designing and prototyping these systems. A greater adhesive thickness was found to decrease the single-hit performance of ceramic/metal armors.

3. Manufacturing defects in the form of trapped air bubbles/voids within the adhesive layer were simulated by randomly deleting elements. An increase in the amount of defects resulted in a decrease of armor performance. This suggests when manufacturing these armor systems, more attention should be invested in quality control checks to ensure the armor will perform optimally.
4. This thesis determines loss tangent input values as a function of wavelength (due to the ionic mechanisms of the material) for the infrared regime, which, in turn, is also used to validate the polyethylene material model.
5. This thesis provides efficient micro- and macro-scale polyethylene-based metamaterial designs used for infrared signature management applications. A macro-scale lenticular lens design (single sheet and sandwiched structures) is proposed for a more passive form of camouflage due to its emissive stability under varying geometrical configurations (e.g., lens radii and air gap thicknesses for sandwiched configurations). In addition, a micro-scale post design is proposed for highly-customizable IR emitting surfaces under passive and active (strain actuated) forms of modulation.

## 4.2 Future work and recommendations

To build upon the current work of this thesis, possible research directions are outlined below:

- *Modelling void growth prior to crack propagation* - The current adhesive model implemented in this thesis predicts crack initiation and crack growth. To im-

prove upon this model, a Gurson-Tvergaard-Needleman (GTN) model can be coupled with the cohesive zone method to predict void growth within the adhesive layer prior to crack growth and interface debonding [112]. This would allow the model to capture a finer time-scale and enables a more accurate prediction of impact failure performance of armor systems incorporating adhesive materials.

- *Developing functional relationships between material and geometrical properties for the adhesive model* - The current adhesive model considers the dependency of the adhesive thickness on modes I and II critical energy release rates. In addition to this dependency, it has been found that the ratio of the area under the ductility plateau curve to the entire area of the traction separation curve increases and the initial stiffness and peak traction decrease with increasing adhesive thickness [35]. A functional relationship between these material properties and the thickness of the adhesive needs to be developed and implemented in the model.
- *Considering visco-elasto-plasticity in the adhesive model* - The proposed adhesive model considers strain rate effects but does not capture thermal effects, strain softening, and hardening of the adhesive polymer during impact. To consider these effects, a thermo-visco-elasto-plastic model [113, 114] under compression, shear, and tension loading can be developed via a user subroutine. This model would capture the important mechanisms of high-velocity impact loading on adhesives, and can lead to further model development to include phase transformation through crystallization [115, 116].
- *Shock modelling in polymers* - The adhesive model can be further expanded to consider shock and corresponding stress wave propagation across the adhesive layer [117–120]. The dynamic failure and performance of armor systems can be tuned by controlling the wave magnitudes and propagations by exploring

various mechanical (e.g., material selection) and geometrical properties (e.g., ceramic tile shape and layer configuration) of the armor design for optimum performance.

- *Full-system scale armor model* - A system-scale armor model is currently being developed where the geometry generation is automated by: (1) varying the dimensions of each of the hexagonal ceramic tiles with a tolerance error of  $\pm 2\%$ , (2) randomly filling gaps between the ceramic tiles with the polyurethane adhesive material, and (3) assigning random Johnson-Holmquist 2 material model parameters and pre-damaged values (between 0 and 0.5) to some of the ceramic tiles to simulate initial damage caused by manufacturing processes. The resulting codes and meshes have been developed by the author of this thesis and are currently used by other students to build a full-scale armor model. This work is still in progress and therefore is not included in this thesis.
- *Developing predictive models for radiative thermoregulating multi-material systems* - Validate and incorporate multi-layered and multi-material predictive models (consisting of pigmented dyes, polymers, and thin metallic foils) for thermal radiation control.
- *Relationship between optical properties and infrared signature management capabilities* - Evaluate functional forms between optical properties (such as emissivity, reflectivity, and transmissivity) and infrared camouflage capabilities (e.g., apparent temperatures and heat signatures) that are to define optical performance.

# Bibliography

- [1] A Rashed, M Yazdani, A. Babaluo, and P. H. Parvin, “Investigation on high-velocity impact performance of multi-layered alumina ceramic armors with polymeric interlayers,” *Journal of Composite Materials*, vol. 50, no. 25, pp. 3561–3576, 2016.
- [2] A. Prakash, J. Rajasankar, N. Anandavalli, M. Verma, and N. R. Iyer, “Influence of adhesive thickness on high velocity impact performance of ceramic/metal composite targets,” *International Journal of Adhesion and Adhesives*, vol. 41, pp. 186–197, 2013.
- [3] W. Seifert, E. Strassburger, S. Grefen, and S. Schaare, “Experimental study about the influence of adhesive stiffness to the bonding strengths of adhesives for ceramic/metal targets,” *Defence Technology*, vol. 12, no. 2, pp. 188–200, 2016, 2016 International Symposium on Ballistics.
- [4] Y. Shen, Y. Wang, S. Du, Z. Yang, H. Cheng, and F. Wang, “Effects of the adhesive layer on the multi-hit ballistic performance of ceramic/metal composite armors,” *Journal of Materials Research and Technology*, vol. 13, pp. 1496–1508, 2021.
- [5] A. Harris, B Vaughan, J. Yeomans, P. Smith, and S. Burnage, “Surface preparation of silicon carbide for improved adhesive bond strength in armour applications,” *Journal of the European Ceramic Society*, vol. 33, no. 15-16, pp. 2925–2934, 2013.
- [6] A. Serjouei, R. Chi, Z. Zhang, and I. Sridhar, “Experimental validation of blv model on bi-layer ceramic-metal armor,” *International Journal of Impact Engineering*, vol. 77, pp. 30–41, 2015.
- [7] A. L. Florence, “Interaction of projectiles and composite armor. part ii,” STANFORD RESEARCH INST MENLO PARK CA, Tech. Rep., 1969.
- [8] Z Rozenberg and Y Yeshurun, “The relation between ballastic efficiency and compressive strength of ceramic tiles,” *International journal of impact engineering*, vol. 7, no. 3, pp. 357–362, 1988.
- [9] Y. Gao, W. Zhang, P. Xu, X. Cai, and Z. Fan, “Influence of epoxy adhesive layer on impact performance of tib2-b4c composites armor backed by aluminum plate,” *International Journal of Impact Engineering*, vol. 122, pp. 60–72, 2018.

- [10] R. Zaera, S. Sánchez-Sáez, J. Pérez-Castellanos, and C. Navarro, “Modelling of the adhesive layer in mixed ceramic/metal armours subjected to impact,” *Composites Part A: Applied Science and Manufacturing*, vol. 31, no. 8, pp. 823–833, 2000.
- [11] H. Zhu *et al.*, “High-temperature infrared camouflage with efficient thermal management,” *Light: Science & Applications*, vol. 9, no. 1, pp. 1–8, 2020.
- [12] T. Kim, J.-Y. Bae, N. Lee, and H. H. Cho, “Hierarchical metamaterials for multispectral camouflage of infrared and microwaves,” *Advanced Functional Materials*, vol. 29, no. 10, p. 1807319, 2019.
- [13] N. Lee *et al.*, “Multiple resonance metamaterial emitter for deception of infrared emission with enhanced energy dissipation,” *ACS Applied Materials & Interfaces*, vol. 12, no. 7, pp. 8862–8869, 2020.
- [14] J. Mason, S. Smith, and D. Wasserman, “Strong absorption and selective thermal emission from a midinfrared metamaterial,” *Applied Physics Letters*, vol. 98, no. 24, p. 241105, 2011.
- [15] D. M. Nguyen, H. Xu, Y. Zhang, and B. Zhang, “Active thermal cloak,” *Applied Physics Letters*, vol. 107, no. 12, p. 121901, 2015.
- [16] L. Long, S. Taylor, X. Ying, and L. Wang, “Thermally-switchable spectrally-selective infrared metamaterial absorber/emitter by tuning magnetic polariton with a phase-change vo2 layer,” *Materials Today Energy*, vol. 13, pp. 214–220, 2019.
- [17] N. Lee, J.-S. Lim, I. Chang, D. Lee, and H. H. Cho, “Transparent metamaterials for multispectral camouflage with thermal management,” *International Journal of Heat and Mass Transfer*, vol. 173, p. 121173, 2021.
- [18] M. Yaman *et al.*, “Arrays of indefinitely long uniform nanowires and nanotubes,” *Nature materials*, vol. 10, no. 7, pp. 494–501, 2011.
- [19] Y. Kai, “Femtosecond laser textured porous nanowire structured glass for enhanced thermal imaging,” 2022.
- [20] S. Hanauer *et al.*, “Transparent and mechanically resistant silver-nanowire-based low-emissivity coatings,” *ACS Applied Materials & Interfaces*, vol. 13, no. 18, pp. 21971–21978, 2021.
- [21] N. Lee, J.-S. Lim, I. Chang, D. Lee, and H. H. Cho, “Flexible thermocamouflage materials in supersonic flowfields with selective energy dissipation,” *ACS Applied Materials & Interfaces*, vol. 13, no. 36, pp. 43524–43532, 2021.
- [22] H. Zhu *et al.*, “Multispectral camouflage for infrared, visible, lasers and microwave with radiative cooling,” *Nature communications*, vol. 12, no. 1, pp. 1–8, 2021.
- [23] X. He and L. Wu, “Illusion thermodynamics: A camouflage technique changing an object into another one with arbitrary cross section,” *Applied Physics Letters*, vol. 105, no. 22, p. 221904, 2014.

- [24] S. Dang and H. Ye, “A visible-infrared-compatible camouflage photonic crystal with heat dissipation by radiation in 5–8  $\mu\text{m}$ ,” *Cell Reports Physical Science*, vol. 2, no. 11, p. 100617, 2021.
- [25] Y. Li, X. Bai, T. Yang, H. Luo, and C.-W. Qiu, “Structured thermal surface for radiative camouflage,” *Nature communications*, vol. 9, no. 1, pp. 1–7, 2018.
- [26] T. Faneco, R. Campilho, and R. Lopes, “Strength and fracture characterization of a novel polyurethane adhesive for the automotive industry,” *Journal of Testing and Evaluation*, vol. 45, pp. 398–407, Mar. 2017.
- [27] S. Marzi, O. Hesebeck, M. Brede, and F. Kleiner, “A rate-dependent , elasto-plastic cohesive zone mixed-mode model for crash analysis of adhesively bonded joints,” 2009.
- [28] M. Chen, A. M. Morsy, and M. L. Povinelli, “Design of VO<sub>2</sub>-coated silicon microspheres for thermally-regulating paint,” *Optics Express*, vol. 27, no. 15, pp. 21787–21793, 2019.
- [29] H. Pisavadia, G. Toussaint, P. Dolez, and J. D. Hogan, “Cohesive zone failure modelling of polymeric adhesives used in ceramic/metal armor,” *International Journal of Impact Engineering*, p. 104364, 2022.
- [30] M. Grujicic, B. Pandurangan, and B. d’Entremont, “The role of adhesive in the ballistic/structural performance of ceramic/polymer–matrix composite hybrid armor,” *Materials Design*, vol. 41, pp. 380–393, 2012.
- [31] K. Chatzikypraios, *Advanced technologies for the bonding and de-bonding of armour structures (armourbond)*, 2019.
- [32] J. Puente, A. Arias, R. Zaera, and C. Navarro, “The effect of the thickness of the adhesive layer on the ballistic limit of ceramic/metal armors. an experimental and numerical study,” *International Journal of Impact Engineering*, vol. 32, Dec. 2005.
- [33] K. Arslan and R. Gunes, “Ballistic impact simulation of ceramic/metal armor structures,” *Uluslararası Muhendislik Arastırma ve Gelistirme Dergisi*, pp. 12–18, Dec. 2017.
- [34] S. Marzi, “An extension of MAT 240 to consider the failure of structural adhesive joints in crash simulations,” in *German LS-Dyna Forum, conference proceedings, Bamberg*, 2010.
- [35] B. Watson, M. J. Worswick, and D. S. Cronin, “Quantification of mixed mode loading and bond line thickness on adhesive joint strength using novel test specimen geometry,” *International Journal of Adhesion and Adhesives*, vol. 102, p. 102682, 2020.
- [36] D. Bürger, A. Rocha de Faria, S. F. de Almeida, F. C. de Melo, and M. V. Donadon, “Ballistic impact simulation of an armour-piercing projectile on hybrid ceramic/fiber reinforced composite armours,” *International Journal of Impact Engineering*, vol. 43, pp. 63–77, 2012.

- [37] G. Akhmet, Y. Yu, P. Hu, W. bin Hou, and X. Han, “Analysis of the performance of adhesively bonded corrugated core sandwich structures using cohesive zone method,” *Journal of Sandwich Structures & Materials*, vol. 22, no. 1, pp. 104–124, 2020. eprint: <https://doi.org/10.1177/1099636217732530>.
- [38] A. Guilpin, G. Franciere, L. Barton, M. Blacklock, and M. Birkett, “A numerical and experimental study of adhesively-bonded polyethylene pipelines,” *Polymers*, vol. 11, no. 9, 2019.
- [39] M. Gurvich, “Fracture modeling and characterization of elastomeric materials and composites for design applications,” *Rubber Chemistry and Technology*, vol. 83, pp. 368–379, Dec. 2010.
- [40] D. Silva, R. Campilho, and U. Carvalho, “Application a direct/cohesive zone method for the evaluation of scarf adhesive joints,” *Applied Adhesion Science*, vol. 6, Dec. 2018.
- [41] L. Hamitouche, M. Tarfaoui, and A. Vautrin, “An interface debonding law subject to viscous regularization for avoiding instability: Application to the delamination problems,” *Engineering Fracture Mechanics*, vol. 75, no. 10, pp. 3084–3100, 2008.
- [42] A. Maziz, M. Tarfaoui, S. Rechak, M. Nachtane, and L. Gemi, “Finite element analysis of impact-induced damage in pressurized hybrid composites pipes,” *Int. J. Appl. Mech*, vol. 13, p. 2150074, 2021.
- [43] A. Maziz, M. Tarfaoui, L. Gemi, S. Rechak, and M. Nachtane, “A progressive damage model for pressurized filament-wound hybrid composite pipe under low-velocity impact,” *Composite Structures*, vol. 276, p. 114520, 2021.
- [44] I. Goda and J. Girardot, “Numerical modeling and analysis of the ballistic impact response of ceramic/composite targets and the influence of cohesive material parameters,” *International Journal of Damage Mechanics*, vol. 30, no. 7, pp. 1079–1122, 2021.
- [45] Z. Jia, G. Yuan, X. Feng, and Y. Zou, “Numerical study on the mechanical behavior of a polyurethane adhesive under high strain rate,” *Composites Part B: Engineering*, vol. 158, pp. 131–140, 2019.
- [46] *LS-DYNA version 11.1*, <https://www.lstc.com/products/ls-dyna>, Livermore Software Technology Corporation, 2007.
- [47] J. Lemaitre and R. Desmorat, “Engineering damage mechanics: Ductile, creep, fatigue and brittle failures,” in Springer Nature, 2005, ch. 1, pp. 1–76.
- [48] “The mathematical theory of plasticity,” in *Computational Methods for Plasticity*. John Wiley Sons, Ltd, 2008, ch. 6, pp. 137–190. eprint: <https://onlinelibrary.wiley.com/doi/pdf/10.1002/9780470694626.ch6>.
- [49] S. Cardamone, A. Bernasconi, and M. Giglio, “Characterization of the 3m scotch-weld™ 7260 b/a epoxy adhesive by cohesive damage models and application to a full-scale bonded sub-structure,” *The Journal of Adhesion*, vol. 96, pp. 1270–1301, Oct. 2020.

- [50] *Sikaforce-7752 frw l60*, Version 1, <https://deu.sika.com/de/industrie/marine/ kleben- und- dichtenimboots- undschiffbau/sandwichpaneele- undmoebelteile/ sikaforce-472-frl60.html>, Sika Industry, Jun. 2013.
- [51] Y. B. Liu, “Application of a rate dependent cohesive zone model to predict impact response in adhesively bonded ultra-high strength steel tubes,” M.S. thesis, University of Waterloo, 2019.
- [52] L. Shengze, F. Jin, Z. Weihua, and X. Meng, “Research of hail impact on aircraft wheel door with lattice hybrid structure,” *Journal of Physics: Conference Series*, vol. 744, p. 012 102, Sep. 2016.
- [53] *LS-DYNA Keyword User’s Manual*, <https://www.dynasupport.com/manuals>, Livermore Software Technology Corporation, 2007.
- [54] C. Desai, S. Basu, and V. Parameswaran, “Determination of traction separation law for interfacial failure in adhesive joints at different loading rates,” *The Journal of Adhesion*, vol. 92, p. 150 527 102 921 008, May 2015.
- [55] R. Fernandes and R. Campilho, “Testing different cohesive law shapes to predict damage growth in bonded joints loaded in pure tension,” *The Journal of Adhesion*, vol. 93, Mar. 2016.
- [56] A. Guilpin, G. Franciere, L. Barton, M. Blacklock, and M. Birkett, “A numerical and experimental study of adhesively-bonded polyethylene pipelines,” *Polymers*, vol. 11, no. 9, 2019.
- [57] *Hyperworks*, <https://www.altair.com/hyperworks/>, Altair Engineering Incorporation, 2021.
- [58] “A constitutive model and data for metals subjected to large strains, high strain rates and high temperatures,” *Proceedings of the Seventh International Symposium on Ballistics*, 1983.
- [59] G. R. Johnson and T. J. Holmquist, “An improved computational constitutive model for brittle materials,” in *High-pressure Science and technology - 1993*, ser. American Institute of Physics Conference Series, vol. 309, 1994, pp. 981–984.
- [60] D. Cronin, K. Bui, C. Kaufmann, G. McIntosh, and T. Berstad, “Implementation and validation of the Johnson-Holmquist ceramic material model in LS-DYNA,” *4th European LS-DYNA Users Conference*, pp. 47–60, Jan. 2003.
- [61] E. Flores-Johnson, L. Shen, I. Guiamatsia, and G. D. Nguyen, “Numerical investigation of the impact behaviour of bioinspired nacre-like aluminium composite plates,” *Composites Science and Technology*, vol. 96, pp. 13–22, 2014.
- [62] D. Luo, Y. Wang, F. Wang, H. Cheng, B. Zhang, and Y. Zhu, “The influence of metal cover plates on ballistic performance of silicon carbide subjected to large-scale tungsten projectile,” *Materials Design*, vol. 191, p. 108 659, 2020.
- [63] R. Chi, A. Serjouei, I. Sridhar, and G. E. Tan, “Ballistic impact on bi-layer alumina/aluminium armor: A semi-analytical approach,” *International Journal of Impact Engineering*, vol. 52, pp. 37–46, 2013.

- [64] G. Toussaint and I. Polyzois, “Steel spheres impact on alumina ceramic tiles:experiments and finite element simulations,” *International Journal of Applied Ceramic Technology*, vol. 16, Jun. 2019.
- [65] A. Bhattacharjee, A. Bhaduri, R. C. Hurley, and L. Graham-Brady, “Failure Modeling and Sensitivity Analysis of Ceramics Under Impact,” *Journal of Applied Mechanics*, vol. 88, no. 5, Feb. 2021, 051007. eprint: [https://asmedigitalcollection.asme.org/appliedmechanics/article-pdf/88/5/051007/6642894/jam\\\_88\\\_5\\\_051007.pdf](https://asmedigitalcollection.asme.org/appliedmechanics/article-pdf/88/5/051007/6642894/jam\_88\_5\_051007.pdf).
- [66] W. L. Goh, B Luo, W Xu, and Y. Jianming, “Simulation study on influence of component thickness on dwell-penetration transition time of long rod projectile impacting ceramic armour module,” *Journal of Physics: Conference Series*, vol. 1721, p. 012015, Jan. 2021.
- [67] A. B. Dresch, J. Venturini, S. Arcaro, O. R. Montedo, and C. P. Bergmann, “Ballistic ceramics and analysis of their mechanical properties for armour applications: A review,” *Ceramics International*, vol. 47, no. 7, Part A, pp. 8743–8761, 2021.
- [68] B. Koch, P. Jannotti, D. Mallick, B. Schuster, T. Sano, and J. Hogan, “Influence of microstructure on the impact failure of alumina,” *Materials Science and Engineering: A*, vol. 770, p. 138549, Oct. 2019.
- [69] D. F. Gordon, B. Hafizi, Y Khine, and S. Douglass, “Ballistics modeling for non-axisymmetric hypervelocity smart bullets,” NAVAL RESEARCH LAB WASHINGTON DC BEAM PHYSICS BRANCH, Tech. Rep., 2014.
- [70] G. H. Yoon, J. S. Mo, K. H. Kim, C. H. Yoon, and N. H. Lim, “Investigation of bullet penetration in ballistic gelatin via finite element simulation and experiment,” *Journal of Mechanical Science and Technology*, vol. 29, no. 9, pp. 3747–3759, 2015.
- [71] A. M. Soydan, B. Tunaboğlu, A. G. Elsabagh, A. K. Sarı, and R. Akdeniz, “Simulation and experimental tests of ballistic impact on composite laminate armor,” *Advances in materials science and engineering*, vol. 2018, 2018.
- [72] G. Mo, Q. Ma, Y. Jin, W. Yan, Z. Li, and Z. Wu, “Delamination process in cross-ply UHMWPE laminates under ballistic penetration,” *Defence Technology*, vol. 17, no. 1, pp. 278–286, 2021.
- [73] J. M. A. Reina, J. J. N. Prieto, and C. A. García, “Influence of the surface finish on the shear strength of structural adhesive joints and application criteria in manufacturing processes,” *The Journal of Adhesion*, vol. 85, no. 6, pp. 324–340, 2009. eprint: <https://doi.org/10.1080/00218460902880164>.
- [74] M. Martínez, I. Chocron, J. Rodríguez, V. Sánchez Gálvez, and L. Sastre, “Confined compression of elastic adhesives at high rates of strain,” *International Journal of Adhesion and Adhesives*, vol. 18, no. 6, pp. 375–383, 1998.

- [75] M. Lißner, E. Alabort, B. Erice, H. Cui, and N. Petrinic, “A rate dependent experimental and numerical analysis of adhesive joints under different loading directions,” *The European Physical Journal Special Topics*, vol. 227, pp. 85–97, Sep. 2018.
- [76] A. Butler and C. Argyropoulos, “Mechanically tunable radiative cooling for adaptive thermal control,” *Applied Thermal Engineering*, vol. 211, p. 118527, 2022.
- [77] Y. Rao *et al.*, “Ultra-wideband transparent conductive electrode for electrochromic synergistic solar and radiative heat management,” *ACS Energy Letters*, vol. 6, no. 11, pp. 3906–3915, 2021.
- [78] A. Kazemi Moridani, R. Zando, W. Xie, I. Howell, J. J. Watkins, and J.-H. Lee, “Plasmonic thermal emitters for dynamically tunable infrared radiation,” *Advanced Optical Materials*, vol. 5, no. 10, p. 1600993, 2017.
- [79] H. R. Seyf and A. Henry, “Thermophotovoltaics: A potential pathway to high efficiency concentrated solar power,” *Energy & Environmental Science*, vol. 9, no. 8, pp. 2654–2665, 2016.
- [80] B. Fang *et al.*, “Bidirectional mid-infrared communications between two identical macroscopic graphene fibres,” *Nature communications*, vol. 11, no. 1, pp. 1–9, 2020.
- [81] Y. Liu *et al.*, “Dynamic thermal camouflage via a liquid-crystal-based radiative metasurface,” *Nanophotonics*, vol. 9, no. 4, pp. 855–863, 2020.
- [82] L. Li *et al.*, “Ultrathin titanium carbide (mxene) films for high-temperature thermal camouflage,” *Advanced Functional Materials*, vol. 31, no. 35, p. 2101381, 2021.
- [83] Q. Kang, D. Li, K. Guo, J. Gao, and Z. Guo, “Tunable thermal camouflage based on gst plasmonic metamaterial,” *Nanomaterials*, vol. 11, no. 2, p. 260, 2021.
- [84] T. Inoue, M. D. Zoysa, T. Asano, and S. Noda, “Realization of dynamic thermal emission control,” *Nature materials*, vol. 13, no. 10, pp. 928–931, 2014.
- [85] G. Cai *et al.*, “Diphyllia grayi-inspired stretchable hydrochromics with large optical modulation in the visible–near-infrared region,” *ACS applied materials & interfaces*, vol. 10, no. 43, pp. 37685–37693, 2018.
- [86] C. Xu, M. Colorado Escobar, and A. A. Gorodetsky, “Stretchable cephalopod-inspired multimodal camouflage systems,” *Advanced Materials*, vol. 32, no. 16, p. 1905717, 2020.
- [87] P. Chandrasekhar *et al.*, “Large, switchable electrochromism in the visible through far-infrared in conducting polymer devices,” *Advanced Functional Materials*, vol. 12, no. 2, pp. 95–103, 2002.
- [88] M. A. Kats *et al.*, “Vanadium dioxide as a natural disordered metamaterial: Perfect thermal emission and large broadband negative differential thermal emittance,” *Physical Review X*, vol. 3, no. 4, p. 041004, 2013.

- [89] N. Lee, T. Kim, J.-S. Lim, I. Chang, and H. H. Cho, “Metamaterial-selective emitter for maximizing infrared camouflage performance with energy dissipation,”
- [90] T. Shi, Z. Zheng, H. Liu, D. Wu, and X. Wang, “Flexible and foldable composite films based on polyimide/phosphorene hybrid aerogel and phase change material for infrared stealth and thermal camouflage,” *Composites Science and Technology*, vol. 217, p. 109 127, 2022.
- [91] R. Xu, W. Wang, and D. Yu, “A novel multilayer sandwich fabric-based composite material for infrared stealth and super thermal insulation protection,” *Composite Structures*, vol. 212, pp. 58–65, 2019.
- [92] A. Choe *et al.*, “Stimuli-responsive micro/nanoporous hairy skin for adaptive thermal insulation and infrared camouflage,” *Materials Horizons*, vol. 7, no. 12, pp. 3258–3265, 2020.
- [93] T. Han, X. Bai, J. T. Thong, B. Li, and C.-W. Qiu, “Full control and manipulation of heat signatures: Cloaking, camouflage and thermal metamaterials,” *Advanced Materials*, vol. 26, no. 11, pp. 1731–1734, 2014.
- [94] H. Kocer *et al.*, “Intensity tunable infrared broadband absorbers based on vo2 phase transition using planar layered thin films,” *Scientific reports*, vol. 5, no. 1, pp. 1–7, 2015.
- [95] S. Walia *et al.*, “Flexible metasurfaces and metamaterials: A review of materials and fabrication processes at micro-and nano-scales,” *Applied Physics Reviews*, vol. 2, no. 1, p. 011 303, 2015.
- [96] COMSOL AB, Stockholm, Sweden, *COMSOL Multiphysics v. 5.6*, version v. 5.6, Jul. 28, 2022.
- [97] G. Wu and D. Yu, “Preparation and characterization of a new low infrared-emissivity coating based on modified aluminum,” *Progress in Organic Coatings*, vol. 76, no. 1, pp. 107–112, 2013.
- [98] J. Yang, X. Zhang, X. Zhang, L. Wang, W. Feng, and Q. Li, “Beyond the visible: Bioinspired infrared adaptive materials,” *Advanced Materials*, vol. 33, no. 14, p. 2 004 754, 2021.
- [99] L. M. Degenstein, D. Sameoto, J. D. Hogan, A. Asad, and P. I. Dolez, “Smart textiles for visible and ir camouflage application: State-of-the-art and micro-fabrication path forward,” *Micromachines*, vol. 12, no. 7, p. 773, 2021.
- [100] I. D. Peggs, B. Schmucker, and P. Carey, “Assessment of maximum allowable strains in polyethylene and polypropylene geomembranes,” in *Waste containment and remediation*, 2005, pp. 1–16.
- [101] *Rf module user’s guide*, English, version COMSOL 5.3, COMSOL, 2017, 218 pp., November 16, 2011.
- [102] P.-M. Robitaille, “Kirchhoff’s law of thermal emission: 150 years,” *Progr. Phys.*, vol. 4, pp. 3–13, 2009.

- [103] Z. J. Coppens and J. G. Valentine, “Spatial and temporal modulation of thermal emission,” *Advanced Materials*, vol. 29, no. 39, p. 1701275, 2017.
- [104] J. Kim, C. Park, and J. W. Hahn, “Metal–semiconductor–metal metasurface for multiband infrared stealth technology using camouflage color pattern in visible range,” *Advanced Optical Materials*, vol. 10, no. 6, p. 2101930, 2022.
- [105] A. Arya and A. L. Sharma, “Effect of salt concentration on dielectric properties of li-ion conducting blend polymer electrolytes,” *Journal of Materials Science: Materials in Electronics*, vol. 29, no. 20, pp. 17903–17920, 2018.
- [106] N. H. Ismail and M. Mustapha, “A review of thermoplastic elastomeric nanocomposites for high voltage insulation applications,” *Polymer Engineering & Science*, vol. 58, no. S1, E36–E63, 2018.
- [107] P. Zhao, H. Chen, B. Li, H. Tian, D. Lai, and Y. Gao, “Stretchable electrochromic devices enabled via shape memory alloy composites (smac) for dynamic camouflage,” *Optical Materials*, vol. 94, pp. 378–386, 2019.
- [108] C.-Y. Zhang, H.-F. Cheng, Z.-H. Chen, and W.-W. Zheng, “Analysis of polarimetric scattering for backgrounds and camouflage materials,” in *International Symposium on Photoelectronic Detection and Imaging 2009: Advances in Infrared Imaging and Applications*, SPIE, vol. 7383, 2009, pp. 202–208.
- [109] K. Gupta, A. Nishkam, and N. Kasturiya, “Camouflage in the non-visible region,” *Journal of Industrial Textiles*, vol. 31, no. 1, pp. 27–42, 2001.
- [110] H. Yu, G. Xu, X. Shen, X. Yan, and C. Cheng, “Low infrared emissivity of polyurethane/cu composite coatings,” *Applied Surface Science*, vol. 255, no. 12, pp. 6077–6081, 2009.
- [111] H. Jo, J. L. King, K. Blomstrand, and K. Sridharan, “Spectral emissivity of oxidized and roughened metal surfaces,” *International Journal of Heat and Mass Transfer*, vol. 115, pp. 1065–1071, 2017.
- [112] P. Liu, Z. Hu, S. Wang, and W. Liu, “Finite element analysis of the void growth and interface failure of ductile adhesive joints,” *Journal of Failure Analysis and Prevention*, vol. 18, no. 2, pp. 291–303, 2018.
- [113] Z. Wang and P. Li, “Visco-elasto-plastic constitutive model of adhesives under uniaxial compression in a range of strain rates,” *Journal of Applied Polymer Science*, vol. 137, no. 33, p. 48962, 2020.
- [114] G. Antoine and R. Batra, “Low speed impact of laminated polymethylmethacrylate/adhesive/polycarbonate plates,” *Composite Structures*, vol. 116, pp. 193–210, 2014.
- [115] H.-J. Kestenbach, J. Loos, and J. Petermann, “Effect of epitaxial crystallization on adhesive strength in impact-toughened isotactic polypropylene,” *Polymer Engineering & Science*, vol. 38, no. 3, pp. 478–484, 1998.
- [116] V. Ratta, “Crystallization, morphology, thermal stability and adhesive properties of novel high performance semicrystalline polyimides,” Ph.D. dissertation, Virginia Polytechnic Institute and State University, 1999.

- [117] L. Zachary and C. Burger, “Dynamic wave propagation in a single lap joint,” *Experimental Mechanics*, vol. 20, no. 5, pp. 162–166, 1980.
- [118] S. Yildiz, Y. Andreopoulos, R. E. Jensen, D. Shaffren, D. Jahnke, and F. Delale, “Characterization of adhesively bonded aluminum plates subjected to shock-wave loading,” *International Journal of Impact Engineering*, vol. 127, pp. 86–99, 2019.
- [119] R. Ecault, F. Touchard, M. Boustie, L. Berthe, and N. Dominguez, “Numerical modeling of laser-induced shock experiments for the development of the adhesion test for bonded composite materials,” *Composite Structures*, vol. 152, pp. 382–394, 2016.
- [120] M. Grujicic, B. Pandurangan, and B. d’Entremont, “The role of adhesive in the ballistic/structural performance of ceramic/polymer–matrix composite hybrid armor,” *Materials & Design*, vol. 41, pp. 380–393, 2012.
- [121] P. Beaurepaire and G. Schuëller, “Modeling of the variability of fatigue crack growth using cohesive zone elements,” *Engineering Fracture Mechanics*, vol. 78, no. 12, pp. 2399–2413, 2011.
- [122] A. Turon, C. Dávila, P. Camanho, and J. Costa, “An engineering solution for mesh size effects in the simulation of delamination using cohesive zone models,” *Engineering Fracture Mechanics*, vol. 74, no. 10, pp. 1665–1682, 2007.
- [123] R. Campilho, M. Banea, J. Neto, and L. da Silva, “Modelling adhesive joints with cohesive zone models: Effect of the cohesive law shape of the adhesive layer,” *International Journal of Adhesion and Adhesives*, vol. 44, pp. 48–56, 2013.
- [124] S. Song, G. Paulino, and W. Buttlar, “Simulation of crack propagation in asphalt concrete using an intrinsic cohesive zone model,” *Journal Of Engineering Mechanics-Asce*, vol. 132, pp. 1215–, Nov. 2006.
- [125] G. A. Gazonas, “Implementation of the Johnson-Holmquist II (JH-2) constitutive model into DYNA3D,” Army Research Lab Aberdeen Proving Ground MD Weapons and Materials Research Directorate, Tech. Rep., 2002.
- [126] C. Tian, Q. Sun, X. An, P. Ye, and Y. Dong, “Influences of ceramic constraint on protection performances of ceramic-metal hybrid structures under impact loads,” *International Journal of Mechanical Sciences*, vol. 159, pp. 81–90, 2019.
- [127] G. R. Johnson and W. H. Cook, “Fracture characteristics of three metals subjected to various strains, strain rates, temperatures and pressures,” *Engineering Fracture Mechanics*, vol. 21, no. 1, pp. 31–48, 1985.
- [128] Y. Xiao, H. Wu, and X. Ping, “On the simulation of fragmentation during the process of ceramic tile impacted by blunt projectile with sph method in ls-dyna,” *Computer Modeling in Engineering Sciences*, vol. 122, pp. 923–954, Jan. 2020.

# Appendix A: Appendices for Chapter 2

## A.1 Numerical methods

### A.1.1 Cohesive zone model

To develop a dynamic failure model of adhesives, this study used the CZM approach. The cohesive elements represent the region of expected crack growth in the model [121]. These cohesive elements follow the traction separation law (TSL), which is an approximation to the Griffith's theory of crack growth [122]. CZM has an advantage over traditional finite element methods because it offers a better strength and fracture prediction through choosing the best TSL shape for the material [123]. The traction separation law defines cohesive shear and tension stresses with their respective displacements. With a defined TSL, the cohesive zone can predict the initiation and direction of crack growth [124]. This is possible as the calculation involves combining fracture mechanics with stress-based criteria [36].

A trilinear cohesive mixed-mode elasto-plastic rate material model (`*MAT_COHESIVE_MIXED_MODE_ELASTOPLASTIC_RATE`) available in the LS-DYNA software is used in this study to simulate the dynamic failure behavior of adhesively bonded joints. The model follows the trilinear (or trapezoidal) TSL as shown in Fig. A.1. The model considers the effects of plasticity and strain rate dependency, and assumes plastic failure during separation [27]. In Fig. A.1, the area under the TSL represents the critical energy release rate of the material,  $G_C$  (N/m). The plastic region is the constant stress horizontal line which spans up to damage initiation. The area under the horizontal line is denoted by  $G_P$  (N/m). The initial linear portion of the curve assumes the adhesive behaves linear-elastically until the plastic region. Damage is initiated once the plastic region ends, and the adhesive fails when the energy dissipated during crack propagation equals  $G_C$ . Furthermore, the mode I and mode II critical energy release rates,  $G_{IC}$  (N/m) and  $G_{IIC}$  (N/m), are dependent on the adhesive thickness [34]. The relationship between the critical energy release rates and adhesive thickness,  $t_A$  (m), is expressed as [34]:

$$G_{IC} = \gamma_I(1 - e^{-\tau_I t_A}) \quad (\text{A.1})$$

$$G_{IIC} = \gamma_{II}(1 - e^{-\tau_{II} t_A}) \quad (\text{A.2})$$

where  $\gamma_I$  (J/m<sup>2</sup>),  $\gamma_{II}$  (J/m<sup>2</sup>),  $\tau_I$  (1/m), and  $\tau_{II}$  (1/m) are constants determined experimentally. The trilinear TSL is chosen over the bilinear TSL since it has the ability to model plasticity and it is a readily available material model in LS-DYNA [27].

The separations in the peel,  $\Delta_n$  (m), and the shear,  $\Delta_t$  (m), modes are given by

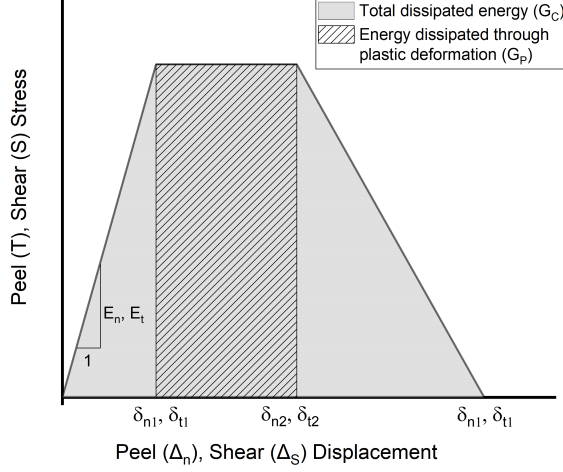


Figure A.1: Trilinear traction separation law used in the cohesive mixed-mode elasto-plastic rate material model in LS-DYNA [46].

[27]:

$$\Delta_n = \langle u_n \rangle \text{ where } \begin{cases} u_n, & \text{if } u_n > 0 \\ 0, & \text{else} \end{cases} \quad (\text{A.3})$$

$$\Delta_t = \sqrt{u_{t1}^2 + u_{t2}^2} \quad (\text{A.4})$$

where  $u_n$  (m),  $u_{t1}$  (m), and  $u_{t2}$  (m) are mode I, II, and III separations, respectively. Mixed-mode separation,  $\Delta_m$  (m), is defined as [27]:

$$\Delta_m = \sqrt{u_n^2 + u_t^2} \quad (\text{A.5})$$

where  $u_t$  (m) is the separation in the shear direction.

The initial stiffnesses of the normal,  $E_n$  (Pa), and tangential,  $E_t$  (Pa), directions are given by [27]:

$$E_n = E/t_{elem} \text{ and } E_t = G/t_{elem} \quad (\text{A.6})$$

where  $E$  (Pa) is the Young's modulus,  $G$  (Pa) is the shear modulus, and  $t_{elem}$  (m) is the user defined element thickness. For loading modes I and II, the shape of the TSL is defined by the ratios  $f_{G1} = G_{IP}/G_{IC}$  and  $f_{G2} = G_{IIP}/G_{IIC}$ , where  $G_{iP}$  (N/m) and  $G_{iC}$  (N/m) are the areas under the plastic region and entire curve for  $i = 1, 2$  for loading modes I and II, respectively [27]. The equivalent strain rate,  $\dot{\epsilon}_{eq}$  (1/s), is calculated by [27]:

$$\dot{\epsilon}_{eq} = \frac{\sqrt{\dot{u}_n^2 + \dot{u}_{t1}^2 + \dot{u}_{t2}^2}}{t_{elem}} \quad (\text{A.7})$$

where  $\dot{u}_n$  (m/s),  $\dot{u}_{t1}$  (m/s), and  $\dot{u}_{t2}$  (m/s) are the velocities in the peel and the two tangential directions, respectively. Tensile,  $T$  (Pa), and shear,  $S$  (Pa), stresses are calculated as functions of the equivalent strain rates by a linear logarithm function (Equation A.8), and constant values (rate independent) (Equation A.9) [27]:

$$\begin{aligned} T(\dot{\epsilon}_{eq}) &= T_0 + T_1 \left( \ln \frac{\dot{\epsilon}_{eq}}{\dot{\epsilon}_T} \right), \text{ if } T_0 < 0, T_1 < 0 \\ S(\dot{\epsilon}_{eq}) &= S_0 + S_1 \left( \ln \frac{\dot{\epsilon}_{eq}}{\dot{\epsilon}_S} \right), \text{ if } S_0 < 0, S_1 < 0 \end{aligned} \quad (\text{A.8})$$

$$\begin{aligned} T(\dot{\epsilon}_{eq}) &= T_0, \text{ if } T_0 > 0 \\ S(\dot{\epsilon}_{eq}) &= S_0, \text{ if } S_0 > 0 \end{aligned} \quad (\text{A.9})$$

where  $S_0$  (Pa) and  $T_0$  (Pa) are the lower bounds of shear and yield strengths, and  $S_1$  (Pa) and  $T_1$  (Pa) are the upper bounds of shear and yield strengths. Similarly, fracture energies in mode I loading,  $G_{IC}$  (Pa/m) and mode II loading,  $G_{IIC}$  (Pa/m) are calculated as being rate-dependent (Equation A.10) and rate independent (Equation A.11) [27]:

$$\begin{aligned} G_{IC}(\dot{\epsilon}_{eq}) &= G_{I0} + (G_{I\infty} - G_{I0}) \exp \frac{\dot{\epsilon}_{GI}}{\dot{\epsilon}_{eq}}, \text{ if } G_{I0} < 0 \\ G_{IIC}(\dot{\epsilon}_{eq}) &= G_{II0} + (G_{II\infty} - G_{II0}) \exp \frac{\dot{\epsilon}_{GII}}{\dot{\epsilon}_{eq}}, \text{ if } G_{II0} < 0 \end{aligned} \quad (\text{A.10})$$

$$\begin{aligned} G_{IC}(\dot{\epsilon}_{eq}) &= G_{I0}, \text{ if } G_{I0} > 0 \\ G_{IIC}(\dot{\epsilon}_{eq}) &= G_{II0}, \text{ if } G_{II0} > 0 \end{aligned} \quad (\text{A.11})$$

where  $G_{I0}$  (Pa/m) and  $G_{II0}$  (Pa/m) are the lower bounds of modes I and II critical energy release rates,  $G_{I\infty}$  (Pa/m) and  $G_{II\infty}$  (Pa/m) are the upper bounds of modes I and II critical energy release rates, and  $\dot{\epsilon}_{GI}$  (1/s) and  $\dot{\epsilon}_{GII}$  (1/s) are the equivalent strain rate at yield initiation to describe the rate dependency of  $G_{IC}$  and  $G_{IIC}$ , respectively. Next, the mixed-mode behavior is evaluated.

The mixed-mode yield initiation,  $\delta_{m1}$  (m), damage initiation,  $\delta_{m2}$  (m), and final displacements,  $\delta_{mf}$  (m), are formulated using a quadratic initiation criterion given by [27]:

$$\delta_{m1} = \delta_{n1} \delta_{t1} \sqrt{\frac{1 + \beta^2}{\delta_{t1}^2 + (\beta \delta_{n1})^2}} \quad (\text{A.12})$$

$$\delta_{m2} = \delta_{n2} \delta_{t2} \sqrt{\frac{1 + \beta^2}{\delta_{t2}^2 + (\beta \delta_{n2})^2}} \quad (\text{A.13})$$

$$\delta_{mf} = \frac{\delta_{m1}(\delta_{m1} - \delta_{m2}) E_n G_{IIC} \cos \gamma^2 + G_{IC} (2G_{IIC} + \delta_{m1}(\delta_{m1} - \delta_{m2}) E_t \sin \gamma^2)}{\delta_{m1} (E_n G_{IIC} \cos \gamma^2 + E_t G_{IC} \sin \gamma^2)} \quad (\text{A.14})$$

where  $\delta_{n1} = \frac{T}{E_n}$  (m) and  $\delta_{t1} = \frac{S}{E_t}$  (m) are the single-mode yield initiation displacements,  $\beta = \frac{\delta_{t1}}{\delta_{n1}}$  is the mixed-mode ratio,  $\delta_{n2} = \delta_{n1} + \frac{f_{G1} G_{IC}}{T}$  (m),  $\delta_{t2} = \delta_{t1} + \frac{f_{G2} G_{IIC}}{S}$  (m) are the single-mode damage initiation displacements, and parameter  $\gamma = \arccos \frac{u_n}{\Delta_m}$ . Plastic separation in the peel direction,  $u_{n,P}$  (m), and the shear elastic separation,  $\delta_{t,y}$  (m), are given by [27]:

$$u_{n,P} = \max(u_{n,P,\Delta t-1}, u_n - \delta_{m1} \sin \gamma, 0) \quad (\text{A.15})$$

$$\delta_{t,y} = \sqrt{(u_{t1} - u_{t1,P,t_i-1})^2 + (u_{t2} - u_{t2,P,t_i-1})^2} \quad (\text{A.16})$$

The plastic shear separations in mode I,  $u_{t1,P}$  (m), and mode II,  $u_{t1,P}$  (m), become: [27]:

$$u_{t1,P} = u_{t1,P,t_{i-1}} + u_{t1} - u_{t1,t_{i-1}} \quad (\text{A.17})$$

$$u_{t2,P} = u_{t2,P,t_{i-1}} + u_{t2} - u_{t2,t_{i-1}} \quad (\text{A.18})$$

when  $\delta_{t,y} > \delta_{m1} \sin \gamma$  and where  $t_{i-1}$  (s) is the previous timestep value.

The damage parameter,  $D_{CZM}$ , is defined as [27]:

$$D_{CZM} = \max \frac{\Delta_m - \delta_{m2}}{\delta_{mf} - \delta_{m2}}, D_{CZM,\Delta t-1}, 0 \quad (\text{A.19})$$

and is initiated once  $\Delta_m > \delta_{m2}$ . The element fully fails ( $D_{CZM} = 1$ ) when  $\Delta_m > \delta_{mf}$ . Once the damage parameter is solved, the peel,  $\sigma_{ti}$  (Pa), and shear stresses,  $\sigma_n$ , are calculated using [27]:

$$\sigma_{t1} = E_t(1 - D_{CZM})(u_{t1} - u_{t1,P}) \quad (\text{A.20})$$

$$\sigma_{t2} = E_t(1 - D_{CZM})(u_{t2} - u_{t1,2}) \quad (\text{A.21})$$

$$\sigma_n = \begin{cases} E_n(1 - D_{CZM})(u_n - u_{n,P}), & \text{if } u_n - u_{n,P} > 0 \\ E_n(u_n - u_{n,P}), & \text{if } u_n - u_{n,P} \leq 0 \end{cases} \quad (\text{A.22})$$

The parameters for this material model are later validated using experimental results from Faneco et al. [26] for the SikaForce<sup>TM6</sup> 7752-L60 polyurethane adhesive. Once validated, this cohesive zone material model is used to simulate the dynamic failure behavior of the polyurethane adhesive bonding a ceramic plate to a metal backing during high-velocity impact conditions.

### A.1.2 Johnson-Holmquist II material model

The Johnson-Holmquist II (JH2) material model (\*MAT\_JOHNSON\_HOLMQUIST\_CERAMICS) is used to model the 99.5% purity alumina ceramic tile of the layered structure [1]. The JH2 model is a popular damage model to represent the behavior of brittle materials subjected to large strains, strain rates, and pressures [59]. Many studies have used the JH2 material model to simulate ceramic tiles undergoing ballistic impact [1, 33, 36, 62, 64].

In the model, the normalized equivalent stress,  $\sigma_{JH2}^*$ , is defined as [125]:

$$\sigma_{JH2}^* = \sigma_{i,JH2}^* - D_{JH2}(\sigma_{i,JH2}^* - \sigma_{f,JH2}^*) \quad (\text{A.23})$$

where  $D_{JH2}$  is a damage parameter bounded within  $0 \leq D_{JH2} \leq 1$ ,  $\sigma_{i,JH2}^*$  is the intact undamaged behavior when  $D_{JH2} = 0$ , and  $\sigma_{f,JH2}^*$  is the damaged behavior when  $D_{JH2} = 1$ . The equivalent stress, and damaged and undamaged behavior are normalized by the Hugoniot Elastic Limit (HEL) to be made dimensionless through [125]:

$$\sigma_{JH2}^* = \frac{\sigma}{\sigma_{HEL}} \quad (\text{A.24})$$

The intact undamaged and damaged behavior are defined as [125]:

$$\sigma_{i,JH2}^* = a_{JH2}(p^* + t^*)^{n_{JH2}}(1 + c_{JH2} \ln \dot{\epsilon}^*) \quad (\text{A.25})$$

$$\sigma_{f,JH2}^* = b_{JH2}(p^*)^{m_{JH2}}(1 + c_{JH2} \ln \dot{\epsilon}^*) \quad (\text{A.26})$$

where  $a_{\text{JH2}}$ ,  $b_{\text{JH2}}$ ,  $c_{\text{JH2}}$  (1/s),  $m_{\text{JH2}}$ , and  $n_{\text{JH2}}$  are material constants,  $\dot{\varepsilon}^*$  is the normalized plastic strain rate, and  $t^*$  and  $p^*$  are normalized maximum tensile hydrostatic pressure and normalized pressure, respectively. The subscripts are used since similar terms are presented later to define Johnson-Cook material model equations. The pressure term,  $p_{\text{JH2}}$  (Pa), and maximum tensile fracture strength,  $t$  (Pa), is normalized by the HEL through [125]:

$$p^* = \frac{p_{\text{JH2}}}{p_{\text{HEL}}} \quad (\text{A.27})$$

$$t^* = \frac{t}{p_{\text{HEL}}} \quad (\text{A.28})$$

The damage parameter,  $D_{\text{JH2}}$ , is accumulated through [125]:

$$D_{\text{JH2}} = \sum \frac{\Delta \varepsilon^p}{\varepsilon_f^p} \quad (\text{A.29})$$

where  $\varepsilon^p$  and  $\varepsilon_f^p$  are the incremental plastic deformation and rate independent plastic strain to fracture, respectively. The plastic strain to fracture,  $\varepsilon_f^p$ , is given by [125]:

$$\varepsilon_f^p = d_1(p^* + t^*)^{d_2} \quad (\text{A.30})$$

where  $d_1$  and  $d_2$  are material constants. Pressure is defined using an equation of state [125]:

$$p_{\text{JH2}} = k_1\mu + k_2\mu^2 + k_3\mu^3 + \Delta p \quad (\text{A.31})$$

where  $k_1$  (Pa),  $k_2$  (Pa), and  $k_3$  (Pa) are experimentally determined constants, and  $\mu_{\text{JH2}}$  and  $\Delta p$  are the excess compression and pressure increment, respectively.  $\Delta p$  is only added once damage begins to accumulate ( $D_{\text{JH2}} > 0$ ). The excess compression,  $\mu$ , and pressure increment,  $\Delta p_{t+\Delta t}$  (Pa), are given by [125]:

$$\mu_{\text{JH2}} = \frac{\rho_{\text{JH2}}}{\rho_{0,\text{JH2}}} - 1 \quad (\text{A.32})$$

$$\Delta p_{t+\Delta t} = -k_1\mu_t + \sqrt{(k_1\mu_t + \Delta p_t)^2 + 2\beta_{\text{JH2}}k_1\Delta U} \quad (\text{A.33})$$

where  $\rho_{0,\text{JH2}}$  (kg/m<sup>3</sup>) and  $\rho_{\text{JH2}}$  (kg/m<sup>3</sup>) are the initial and final densities, respectively,  $\Delta U$  (J) is the incremental energy loss between successive damage states, and  $\beta_{\text{JH2}}$  is the fraction of elastic energy converted to potential energy. The subscript  $t$  (s) is the previous time step and  $t + \Delta t$  (s) is the current time step. In this study, the JH2 material model is used to simulate impact into a 99.5% alumina ceramic plate. The parameters for this model are validated using numerical results of a system-scale armor model taken from the literature [1, 2] and the parameters are provided in Table 2.4.

### A.1.3 Johnson-Cook material model

The Johnson-Cook (JC) material model (\*MAT\_JOHNSON\_COOK) is implemented for both the 7.62 mm surrogate projectile and the aluminum Al5083 H116 metal backing [1]. The JC model is a well-studied phenomenological model describing the behavior of metals undergoing large deformation, high strain rates, and high temperatures [9, 58]. Thus, this model has been widely used to simulate the response of metals undergoing high-velocity impact [1, 9, 36, 64, 126].

In the JC model, the flow stress,  $\sigma_y$  (Pa), is defined as [58]:

$$\sigma_y = \left( a_{\text{JC}} + b_{\text{JC}} \bar{\varepsilon}^{p^{*n_{\text{JC}}}} \right) (1 + c_{\text{JC}} \ln \dot{\varepsilon}^*) (1 - T^{*m_{\text{JC}}}) \quad (\text{A.34})$$

where  $a_{\text{JC}}$  (Pa),  $b_{\text{JC}}$  (Pa),  $c_{\text{JC}}$ ,  $m_{\text{JC}}$ , and  $n_{\text{JC}}$  are material constants,  $\bar{\varepsilon}^{p^*}$  is the effective plastic strain, and  $\dot{\varepsilon}^*$  and  $T^*$  are the effective plastic strain and normalized temperature. These are defined as [58]:

$$\dot{\varepsilon}^* = \frac{\bar{\varepsilon}^{p^*}}{\dot{\varepsilon}_0} \quad (\text{A.35})$$

$$T^* = \frac{T - T_{\text{room}}}{T_{\text{melt}} - T_{\text{room}}} \quad (\text{A.36})$$

where  $\dot{\varepsilon}_0 = 1$  (1/s), and  $T$  (K),  $T_{\text{room}}$  (K), and  $T_{\text{melt}}$  (K) are the current temperature, room temperature, and melting temperature, respectively. The strain at fracture,  $\varepsilon^f$ , is given by [127]:

$$\varepsilon^f = (D_1 + D_2 \exp D_3 \sigma^*) (1 + D_4 \ln \varepsilon^*) (1 + D_5 T^*) \quad (\text{A.37})$$

where  $D_1$  to  $D_5$  are material constants and  $\sigma^*$  is the effective stress defined as [127]:

$$\sigma^* = \frac{p_{\text{JC}}}{\sigma_{\text{eff}}} \quad (\text{A.38})$$

where  $p_{\text{JC}}$  (Pa) and  $\sigma_{\text{eff}}$  (Pa) are the pressure and effective stress terms, respectively. The damage,  $D_{\text{JC}}$ , is accumulated through [127]:

$$D_{\text{JC}} = \sum \frac{\bar{\varepsilon}^{p^*}}{\varepsilon^f} \quad (\text{A.39})$$

where fracture occurs when  $D_{\text{JC}} = 1$ .

The equation of state relating pressure to volume is given by the linear relationship expressed as:

$$P = C_1 \mu_{\text{JC}} \quad (\text{A.40})$$

where  $C_1$  (Pa) is the bulk modulus and  $\mu_{\text{JC}}$  is the excess compression term given by:

$$\mu_{\text{JC}} = \frac{\rho_{\text{JC}}}{\rho_{0,\text{JC}}} - 1 \quad (\text{A.41})$$

where  $\rho_{\text{JC}}$  (kg/m<sup>3</sup>) is the initial density and  $\rho_{0,\text{JC}}$  (kg/m<sup>3</sup>) is the final density. This material model is also used to simulate the high-velocity impact behavior of a steel 4340 projectile and for an aluminum Al5083 H116 metal backing. The parameters for this model are validated using numerical results of a system-scale armor model from the literature [1, 2] and are provided in Table 2.5.

#### A.1.4 Cowper-Symonds strength model

The epoxy adhesive used for the ceramic/armor validation case is described using the Cowper-Symonds strength model following the simulations performed by Prakash et al. [2] and Rashed et al. [1]. Here, the material is described by the Mie-Gruneisen equation of state (\*EOS\_GRUNEISEN) [1], and the density is defined by using the null material model (\*MAT\_NULL). The Mie-Gruneisen equation of state relates pressure and volume at a given temperature. The pressure term is defined as [128]:

$$p = \frac{\rho_0 C^2 \mu (1 + (1 - \frac{\gamma_0}{2})\mu - \frac{a}{2}\mu^2)}{1 + (S_{MG,1} - 1)\mu - S_{MG,2} \frac{\mu^2}{\mu+1} - S_{MG,3} \frac{\mu^3}{(\mu+1)^2}} + (\gamma_0 + a\mu)E \quad (\text{A.42})$$

$$p = \rho_0 C^2 \mu + (\gamma_0 + a\mu)E \quad (\text{A.43})$$

for compressed and expanded solids, respectively, where  $\gamma_0$  is the unitless Gruneisen gamma,  $a$  is a unitless first order volume correction to  $\gamma_0$ ,  $\rho_0$  ( $\text{kg/m}^3$ ) is the material density,  $E$  (Pa) is the elastic modulus,  $C$  and  $S_{MG,1}$  to  $S_{MG,3}$  are the intercept and unitless coefficients to the cubic shock-velocity versus particle velocity curve, respectively, and  $\mu$  is the excess compression term defined in Equation A.41.

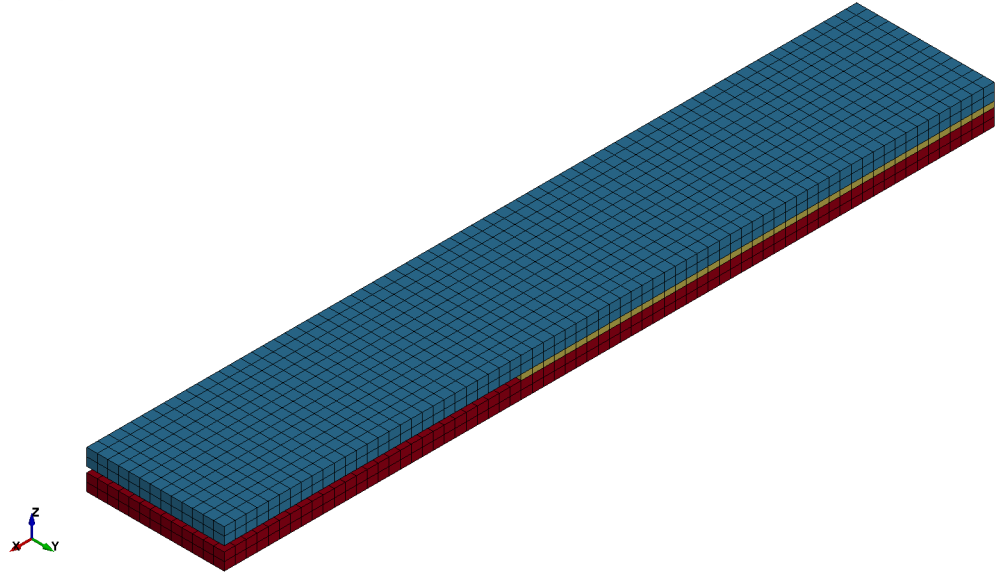
## A.2 Numerical test set up of the double cantilever beam and end-notched flexure tests

A numerical model of the double cantilever beam (DCB) and end-notched flexure (ENF) test setups are created which replicate the experimental work of Faneco et al. [26]. A meshed three-dimensional geometry with element size of 1 mm for the DCB and ENF tests are shown in Fig. A.2. The load is applied 50 mm away from the initial crack region of the adhesive for the DCB test on the top adherend. The hinge is also located 50 mm away from the initial crack region and on the bottom adherend. The hinges for the ENF test are located on the bottom adherend 15 mm inwards from both sides of the test specimen. These hinge placement locations are shown in Fig. A.3 for the DCB and ENF tests and were obtained through correspondence from Faneco et al. [26].

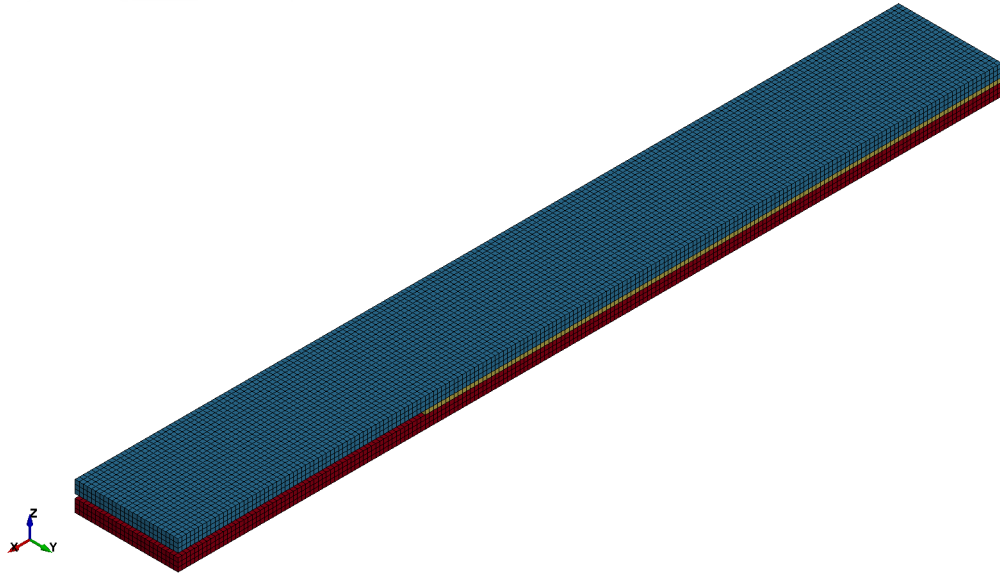
In the simulations, 4-point cohesive elements (termed `ELFORM EQ19` in LS-DYNA) are used for the adhesive layer, and fully integrated hexahedron solid elements (`ELFORM EQ2`) are used for the adherend. An additional contact setting (`*AUTOMATIC_SURFACE_TO_SURFACE`) is needed to define the sliding contact between adherend layers in the ENF test.

## A.3 Element formulation and contact settings for the ceramic/metal armor model

This section discusses element type and the contact settings used for the ceramic/armor model. The element type used for discretization are formulated using the constant stress solid element (`EQ1`). The (`*AUTOMATIC_SURFACE_TO_SURFACE`) is contact is used between the three layers of the ceramic/metal armor model (from Fig. 2.4) where all default values are used. To simulate the erosion of the projectile and the three layers of the composite structure, an eroding surface to surface contact is applied (`*ERODING_SURFACE_TO_SURFACE`) where: (1) the erosion/interior node option (`EROSOP`) is set as 1 to allow for erosion; (2) the adjacent material treatment for solid element (`IADJ`) parameter is set as 1 to allow for self-erosion (erosion between adjacent elements within a single part); (3) the soft constraint option (`SOFT`) is set to 2 for pinball segment based contact to allow for the model to produce contact forces; and (4) the segment-based contact option (`SBOPT`) is set to the recommended value of 3 when setting `SOFT=2`. Lastly, a tied contact (`*TIED_SURFACE_TO_SURFACE`) is applied between the layers of the composite structure to simulate the adhesive bonding where all default values are used.

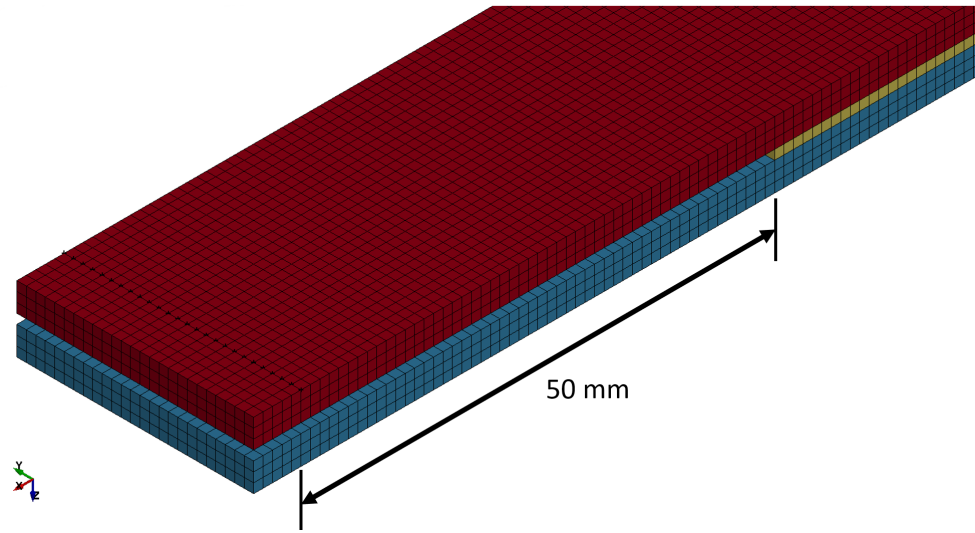


(a)

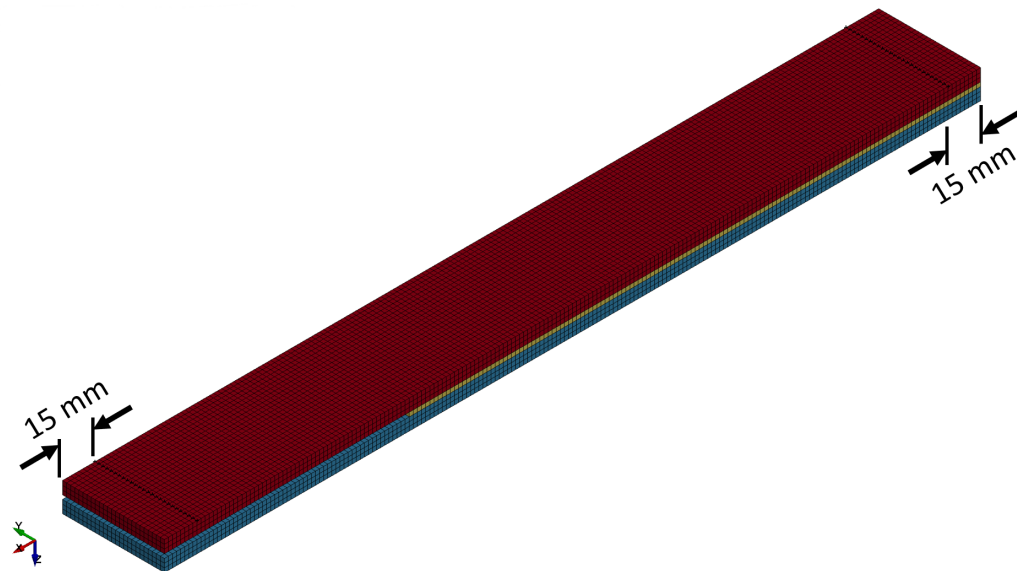


(b)

Figure A.2: Isometric view of the mesh for (a) the double cantilever beam and (b) the end-notched flexure test setups with an element size of 1 mm based on the experimental work performed by Faneco et al. [26].



(a)



(b)

Figure A.3: Hinge placement locations on (a) the double cantilever beam and (b) the end-notched flexure test setups based on the experimental work performed by Faneco et al. [26].